

1 Quantifying energy and water fluxes in dry dune ecosystems of the Netherlands

2

3 B.R. Voortman¹, R.P. Bartholomeus¹, S.E.A.T.M. van der Zee², M.F.P. Bierkens^{3,4}, J.P.M.
4 Witte^{1,5}

5

6 [1] KWR Watercycle Research Institute, P.O. Box 1072, 3430 BB Nieuwegein, the
7 Netherlands

8 [2] Soil Physics and Land Management, Environmental Sciences Group, Wageningen
9 University, P.O. Box 47, 6700 AA Wageningen, the Netherlands

10 [3] Department of Physical Geography, Faculty of Geosciences, Utrecht University, P.O. Box
11 80115, 3508 TC Utrecht, the Netherlands

12 [4] Deltares, P.O. Box 85467, 3508 AL Utrecht, the Netherlands

13 [5] VU University, Institute of Ecological Science, Department of Systems Ecology, de
14 Boelelaan 1085, 1081 HV Amsterdam, the Netherlands

15

16 Correspondence to: bernard.voortman@kwrwater.nl

17

18 Keywords: evapotranspiration, dune, moss, heather, longwave radiation, lysimeter, energy
19 balance, the Netherlands

20 **Abstract**

21 Coastal and inland dunes provide various ecosystem services that are related to groundwater,
22 such as drinking water production and biodiversity. To manage groundwater in a sustainable
23 manner, knowledge of actual evapotranspiration (ET_a) for the various land covers in dunes is
24 essential. Aiming at improving the parameterization of dune vegetation in hydro-
25 meteorological models, this study explores the magnitude of energy and water fluxes in an
26 inland dune ecosystem in the Netherlands. Hydro-meteorological measurements were used to
27 parameterize the Penman-Monteith evapotranspiration model for four different surfaces: bare
28 sand, moss, grass and heather. We found that the net longwave radiation (R_{nl}) was the largest
29 energy flux for most surfaces during daytime. However, modelling this flux by a calibrated
30 FAO-56 R_{nl} model for each surface and for hourly time steps was unsuccessful. Our R_{nl}
31 model, with a novel sub-model using solar elevation angle and air temperature to describe the
32 diurnal pattern in radiative surface temperature, improved R_{nl} simulations considerably.
33 Model simulations of evaporation from moss surfaces showed that the modulating effect of
34 mosses on the water balance is species dependent. We demonstrate that dense moss carpets
35 (*Campylopus introflexus*) evaporate more (5%, +14 mm) than bare sand (total of 258 mm in
36 2013), while more open structured mosses (*Hypnum cupressiforme*) evaporate less (-30%, -76
37 mm) than bare sand. Additionally, we found that a drought event in the summer of 2013
38 showed a pronounced delayed signal on lysimeter measurements of ET_a for the grass and
39 heather surfaces respectively. Due to the desiccation of leaves after the drought event, and
40 their feedback on the surface resistance, the potential evapotranspiration in the year 2013
41 dropped with 9 % (-37 mm) and 10 % (-61 mm) for the grass and heather surfaces
42 respectively, which subsequently led to lowered ET_a of 8 % (-29 mm) and 7 % (-29 mm).
43 These feedbacks are of importance to water resources, especially during a changing climate
44 with increasing number of drought days. Therefore, such feedbacks need to be integrated into
45 a coupled plant physiological and hydro-meteorological model to accurately simulate ET_a . In
46 addition, our study showed that groundwater recharge in dunes can be increased considerably
47 by promoting moss vegetation, especially of open structured moss species.

48

49 **1 Introduction**

50 Coastal and inland sand dunes are major drinking water production sites in the Netherlands.
51 Approximately 23% of Dutch drinking water originates from aquifers in these dunes, which
52 are replenished by both natural groundwater recharge and artificial infiltration of surface
53 waters. Another ecosystem service of groundwater in dune systems is that shallow

54 groundwater tables sustain nature targets with a very high conservation value. Such targets,
55 like wet dune slacks and oligotrophic pools, are often legally enforced, e.g. by the European
56 Habitat Directive and by the Water Framework Directive. Furthermore, a deep layer of fresh
57 groundwater in coastal dunes protects the hinterland from the inflow of saline groundwater.

58 Under a warming climate, summers are expected to become dryer and the water
59 quality of surface waters may degrade (Delpla et al., 2009), especially during dry periods with
60 low river discharge rates (Zwolsman and van Bokhoven, 2007; van Vliet and Zwolsman,
61 2008). To maintain current drinking water quality and production costs, water production in
62 the future may have to rely more on natural groundwater recharge. This implies that drinking
63 water companies need to search for new water production sites or intensify current
64 groundwater extractions, while protecting groundwater dependent nature targets.

65 For sustainable management of renewable groundwater resources, groundwater
66 extractions should be balanced with the amount of precipitation that percolates to the
67 saturated zone, the groundwater recharge. Knowledge of actual evapotranspiration (ET_a , here
68 defined as the sum of plant transpiration, soil evaporation, and evaporation from canopy
69 interception) for the various land covers is essential to quantify the amount of recharge. Inland
70 dune systems are predominantly covered with deciduous and pine forest. Well-developed
71 hydro-meteorological models are available to simulate ET_a for these forest ecosystems
72 (Dolman, 1987; Moors, 2012). Other ecosystems, such as heathland and bare sand colonized
73 by algae, mosses, tussock forming grasses or lichens, received less attention. However,
74 heathland and drift sand ecosystems have a higher conservation value than forest plantations,
75 in particular of coniferous trees. Nature managers are therefore often obligated to protect and
76 develop certain heathland and drift sand ecosystems at the expense of forest ecosystems (The
77 European Natura 2000 policy). A better parameterization of heathland and drift sand
78 ecosystems in hydro-meteorological models would aid in the sustainable management of
79 important groundwater resources and would allow quantifying the cost and benefit of nature
80 conservation in terms of groundwater recharge.

81 To this end, this study explores diurnal patterns in energy and water fluxes in a dry
82 dune ecosystem on an elevated sandy soil in the Netherlands. Our study aims at improving the
83 parameterization of dune vegetation in hydro-meteorological models based on field
84 measurements, focusing on four different surfaces: bare sand, moss (*Campylopus introflexus*),
85 grass (*Agrostis vinealis*) and heather (*Calluna vulgaris*). A second objective is to quantify the
86 effect of moss species on the water balance. Mosses and lichens are present in most
87 successional stages in dry dune ecosystems, either as pioneer species or as understory

88 vegetation. Voortman et al. (2013) hypothesized that moss covered soils could evaporate less
89 than a bare soil, since the unsaturated hydraulic properties of moss layers reduce evaporation
90 under relatively moist conditions. Such hydraulic behavior could have large implications on
91 the ecological interactions between vascular and nonvascular plants in water limited
92 ecosystems, as the presence of a moss cover could facilitate the water availability for rooting
93 plants. Such interactions are of importance to groundwater resources as the resilience of plant
94 communities to drought determines the succession rate and biomass, which subsequently
95 feedback on evapotranspiration.

96 A third objective is to get insight in the delayed effect of dry spells on potential and
97 actual evapotranspiration for heathlands and grasslands. To quantify the evapotranspiration
98 loss term, many hydrological modeling frameworks use the concept of potential
99 evapotranspiration ET_p (Federer et al., 1996; Kay et al., 2013; Zhou et al., 2006), defined as the
100 maximum rate of evapotranspiration from a surface where water is not a limiting factor
101 (Shuttleworth, 2007). ET_p is input to modeling frameworks and reduces to ET_a in cases of
102 water stress. However, if dry spells result in a vegetation dieback, the simulated ET_p should be
103 adjusted to account for the smaller transpiring leaf area after the dry spell. The model
104 simulations presented in this paper give some guidance on the magnitude of errors in
105 simulated ET_a if feedbacks of dry spells on ET_p are neglected.

106 The knowledge presented in this paper will help to improve and interpret the
107 simulations of water recharge in sand dunes by hydrological models, and will sustain
108 rainwater harvesting in dunes by vegetation management.

109

110 **2 Measurements and Methods**

111 **2.1 General setup**

112 A field campaign started in August 2012 to measure energy and water fluxes in the drinking
113 water supply area “Soestduinen”, situated on an elevated sandy soil (an ice-pushed ridge) in
114 the center of the Netherlands (52.14° latitude, 5.31° longitude). Due to deep groundwater
115 levels, the vegetation in this region is groundwater-independent, i.e. relying solely on
116 rainwater (on average 822 mm rain per year, 40% falling in the first 6 months of the year and
117 60% falling in the last 6 months of the year). The reference evapotranspiration according to
118 Makkink (1957) is on average 561 mm per year. The field data was used to parameterize the
119 Penman-Monteith equation, to calculate ET_p , and to perform hydrological model simulations
120 of ET_a , based on the actual availability of soil moisture. The Penman-Monteith equation is
121 given by:

122

123

$$ET_p = \frac{\Delta(R_n - G) + \rho_a c_p (e_s - e_a) / r_a}{\left(\Delta + \gamma \left(1 + \frac{r_s}{r_a} \right) \right) \lambda \rho_w}, \quad 1$$

124

125 where ET_p is the potential evapotranspiration [mm/s], Δ is the slope of the saturation vapor
 126 pressure vs. temperature curve [kPa °C⁻¹], R_n is the net radiation [J m⁻²], G is the soil heat flux
 127 [J m⁻²], ρ_a is the air density [kg m⁻³], c_p is specific heat of moist air [J kg⁻¹ °C⁻¹], e_s is the
 128 saturation vapor pressure of the air [kPa], e_a is the actual vapor pressure of the air [kPa], r_a is
 129 aerodynamic resistance to turbulent heat and vapor transfer [s m⁻¹], γ is the psychrometric
 130 constant [kPa °C⁻¹], λ is the latent heat of vaporization [J kg⁻¹], and ρ_w is the density of liquid
 131 water [kg m⁻³]. Results of Irmak et al. (2005) suggest that estimates of ET_p on hourly time
 132 steps are more accurate than estimates on a daily timescale. Furthermore, Liu et al. (2005)
 133 showed that the use of daily input values leads to a systematic overestimation of ET_a ,
 134 especially for sandy soils. Hence, energy fluxes in the Penman-Monteith equation are
 135 preferably simulated at sub-diurnal timescales. Furthermore, understanding and simulation of
 136 plant physiological processes requires knowledge of the diurnal variation of environmental
 137 variables (Nozue and Maloof, 2006). Therefore, field data was aggregated to hourly time
 138 steps to maintain the diurnal pattern and to analyze our field results at the same time interval
 139 as commonly available climate data.

140

141

142

143

144

145

146

2.2 Hydro-meteorological measurements

147

148

149

150

151

152

153

Four homogeneous sites of bare sand, moss (*Campylopus introflexus*), grass (*Agrostis vinealis*) and heather (*Calluna vulgaris*) (Fig. 2) were selected to measure actual evapotranspiration (ET_a), the net radiation (R_n), the soil heat flux (G) and the albedo. Other meteorological variables such as wind speed (u , at 2 m above the surface), relative humidity (RH , 1.5 m above the surface), air temperature (T_a , 1.5 m above the surface), and rain (P) were measured at a weather station, installed in-between the measurement plots at a maximum distance of 40 m from each plot. Measurements were collected with data loggers

154 (CR1000, Campbell Scientific Inc.) at a 10 second interval and aggregated to minutely values.
155 Field measurements of bare sand, moss and grass were collected between August 2012 and
156 November 2013. The field measurements in the heather vegetation were collected between
157 June 2013 and November 2013.

158 The net radiation was measured with net radiometers (NRLite2 Kip & Zonen B.V.).
159 The net radiometers were installed at a relatively low height of 32, 40, 40, and 50 cm above
160 the bare sand, moss, grass and heather surfaces respectively (relative to the average vegetation
161 height), to limit the field of view to a homogenous surface. The incoming solar radiation ($R_{s\downarrow}$)
162 and reflected solar radiation ($R_{s\uparrow}$) were measured with an albedo meter (CMA6, Kip & Zonen
163 B.V.) that was rotated between the four surfaces. It was installed next to each R_n sensor. Due
164 to a snow cover (winter months) or sensor maintenance (October 2012, May 2013), some
165 periods were omitted (Fig. 3).

166 Eight self-calibrating heat flux plates (HFP01SC, Hukseflux B.V.) (two for each site)
167 were installed at 8 cm below the soil surface near the net radiometers. These heat flux plates
168 were programmed to calibrate themselves for 15 minutes at 6 hour time intervals, based on a
169 known heat flux supplied by an integrated heater. Besides each soil heat flux plate an
170 averaging thermocouple (TCAV, Campbell Scientific, Inc.) was installed at 2 and 6 cm depth
171 and a soil moisture probe (CS616, Campbell Scientific, Inc) was installed at 4 cm depth to
172 estimate the change in heat storage (S) above the heat flux plates. The sum of the measured
173 soil heat flux at 8 cm depth and S represents the heat flux at the soil surface. Sensor
174 installation and procedures to calculate S were followed according to the HFP01SC
175 instruction manual of Campbell Scientific Inc. (2014).

176 Within each surface, one weighing lysimeter was installed. The lysimeters (Fig. 4) had
177 a 47.5 cm inner diameter and were 50 cm deep. Intact soil monoliths were sampled by
178 hammering the PVC tube into the soil, alternated with excavating the surrounding soil to
179 offset soil pressures. The lysimeters were turned upside down, to level the soil underneath and
180 to close this surface with a PVC end cap. To allow water to drain out of the lysimeter bottom
181 plate, a 2.5 cm diameter hole was made in the base plate. A 15 cm long fiberglass wick
182 (Pepperell 2 x ½ inch) was installed in the PVC end cap to guide drainage water through the
183 hole into a tipping bucket (Davis 7852) below the lysimeter. The wick, together with two
184 sheets of filter cloth (140-150 μm , Eijkelkamp Agrisearch Equipment), placed at the bottom
185 of the lysimeter tank, prevented soil particles from flushing out of the lysimeter. The tipping
186 bucket below the lysimeter had a resolution of 0.2 mm for the intercepting area of the tipping

187 bucket, which was equal to 0.024 mm for the cross-sectional area of the lysimeter. Drainage
188 water was collected in a reservoir installed below the lysimeter.

189 The lysimeters were weighted with temperature compensated single point load cells
190 (Utilcell 190i, max 200 kg). These load cells were initially connected to the full bridge data
191 ports of the data loggers. However, the measurement resolution of the data loggers was too
192 coarse to fully compensate for temperature effects on weight measurements. Fluctuations of
193 0.333 μV due to temperature effects were within the data logger measurement resolution,
194 which equals 36 g in weight change, i.e. 0.2 mm of evaporation. To increase the lysimeter
195 precision, digitizers (Flintec LDU 68.1) were installed in May 2013 to process and digitize the
196 load cell signals without interference of the data logger. In this setup, a measurement
197 resolution of 10 g was achieved, i.e. 0.06 mm equivalent water depth, which is adequate for
198 measuring ET_a for daily time periods (subtracting two values would lead to a maximum error
199 of 0.06 mm caused by the measurement resolution). Analysis of measured ET_a were therefore
200 limited to the period after installation of the digitizers.

201 After a rain event on September 7 2013, the tipping buckets below the grass and
202 heather lysimeters became partly clogged with beetles nesting underneath the lysimeters. This
203 led to a continuous drainage signal which was out of phase with the weight measurements.
204 Without accurate drainage measurements, lysimeter weight signals cannot be transferred to
205 evapotranspiration. Therefore, ET_a data on days with a poor drainage signal after September 7
206 2013 were disregarded in the analyses for the grass and heather lysimeters.

207

208 **2.3 Parameterization of the Penman-Monteith equation**

209 **2.3.1 Net radiation (R_n)**

210 The net radiation (R_n) is defined as:

211

$$212 \quad R_n = R_{ns} + R_{nl} = (1 - \text{albedo})R_{s\downarrow} + (\varepsilon_s R_{l\downarrow} - R_{l\uparrow}), \quad 2$$

213

214 where R_{ns} is the net shortwave radiation, R_{nl} is the net longwave radiation, $R_{s\downarrow}$ is the incoming
215 solar radiation, $R_{l\downarrow}$ is the downwelling longwave radiation from the atmosphere to the surface,
216 $R_{l\uparrow}$ is the emitted longwave radiation by the surface into the atmosphere and ε_s is the surface
217 emissivity representing the reflected downwelling longwave radiation. The albedo in Eq. 2
218 was determined by linear regression between measured $R_{s\downarrow}$ and $R_{s\uparrow}$. Based on the albedo
219 obtained this way, R_{nl} follows from measurements of R_n by subtracting calculated R_{ns} from

220 measured R_n . Throughout this paper, this back-calculated R_{nl} is referred to as the measured
221 R_{nl} .

222 In hydro-meteorological models, R_{nl} is commonly estimated under clear sky
223 conditions and multiplied by a factor to correct for clouds (Irmak et al., 2010;Gubler et al.,
224 2012;Blonquist Jr et al., 2010;Temesgen et al., 2007). A similar approach was followed in this
225 study in which the Stefan-Boltzmann law is substituted into Eq. 2 for $R_{l\downarrow}$ and $R_{l\uparrow}$ under clear
226 sky conditions (Saito and Šimůnek, 2009;Van Bavel and Hillel, 1976) and multiplied by a
227 cloudiness function to obtain R_{nl} :

228

$$229 \quad R_{nl} = (\varepsilon_s \varepsilon_a \sigma T_a^4 - \varepsilon_s \sigma T_s^4) f_{cd}, \quad 3$$

230

231 where ε_a is the clear sky emissivity of the atmosphere [-], ε_s is the surface emissivity [-], σ is
232 the Stefan-Boltzmann constant ($5.67 \times 10^{-8} \text{ Wm}^{-2}\text{K}^{-1}$), T_a is the air temperature [K], T_s is the
233 surface temperature [K] and f_{cd} is a cloudiness function [-] (described later). For vegetated
234 surfaces $\varepsilon_s = 0.95$ was used (based on Jones (2004)), and $\varepsilon_s = 0.925$ for bare sand (based on
235 Fuchs and Tanner (1968)). Estimating ε_a has a long history and numerous parameterizations
236 are available. In this study the empirical relationship found by Brunt (1932) was used:

237

$$238 \quad \varepsilon_a = 0.52 + 0.065 \sqrt{e_a}, \quad 4$$

239

240 where e_a is the water vapor pressure measured at screen level [hPa]. The cloudiness function
241 f_{cd} in Eq. 3 is limited to $0.05 \leq f_{cd} \leq 1$ and equal to:

242

$$243 \quad f_{cd} = \frac{R_{s\downarrow}}{R_{s0}}, \quad 5$$

244

245 where R_{s0} is the estimated clear sky solar radiation. We estimated R_{s0} following the FAO
246 irrigation and drainage paper No. 56 (Allen et al., 1998). Since f_{cd} is undefined during the
247 night, an interpolation of f_{cd} between sunset and sunrise is required. According to Gubler et al.
248 (2012) f_{cd} can be best linearly interpolated between the four to six hour average before sunset
249 and after sunrise. We adopted this approach, applying a five-hour average.

250

251 An estimate of T_s is required to fully parameterize Eq. 3. We developed a new
approach to simulate the diurnal pattern in T_s . Using Eq. 3, we back-calculated $T_s - T_a$ based

252 on measured R_{nl} for clear hours ($f_{cd} > 0.9$). Generally, $T_s - T_a$ will be negative during
 253 nighttime (when solar elevation β [radians] < 0), and will gradually increase to positive values
 254 during daytime ($\beta > 0$). We describe this pattern by (Fig. 5):

255

$$256 \quad T_s - T_a = f_{cum}(\beta, \mu_\beta, \sigma_\beta) \left[T_{s,amp} + \beta T_{s,slope} \right] + T_{s,offset}, \quad 6$$

257

258 where f_{cum} is a cumulative normal distribution function with mean μ_β and standard deviation
 259 σ_β , describing the moment at which the surface becomes warmer than the air temperature (μ_β)
 260 and the speed at which the surface warms up or cools down (σ_β) as a function of solar
 261 elevation angle (β). $T_{s,amp}$ is the amplitude of T_s [K], $T_{s,slope}$ is the slope between β and $T_s - T_a$
 262 during daytime [K/radians] and $T_{s,offset}$ is the average value of $T_s - T_a$ during nighttime [K].
 263 The parameters of Eq. 6, except $T_{s,offset}$, were fitted to the data by minimizing the root mean
 264 squared error (*RMSE*) by generalized reduced gradient nonlinear optimization. The $T_{s,offset}$ was
 265 determined as the average nighttime $T_s - T_a$ to limit the amount of parameters during the
 266 optimization. Equation 6 was substituted for T_s in Eq. 3 to estimate R_{nl} . This novel approach
 267 to derive R_{nl} was compared to the R_{nl} model of the FAO-56 approach (Allen et al., 1998),
 268 originally derived to obtain daily estimates of R_{nl} (using minimum and maximum daily T_a
 269 divided by 2 instead of T_a in Eq. 7) but commonly applied at hourly timescales (ASCE-EWRI,
 270 2005; Perera et al., 2015; Gavilán et al., 2008; López-Urrea et al., 2006):

271

$$272 \quad R_{nl} = -\sigma T_a^4 \left(a - b \sqrt{e_a} \right) \left(1.35 \frac{R_s}{R_{s0}} - 0.35 \right), \quad 7$$

273

274 where the first term between brackets represents the net emittance, which should compensate
 275 for the fact that T_s is not measured. The empirical parameters a and b can be calibrated for a
 276 specific climate and/or vegetation. The second term between brackets is a cloudiness function.
 277 The default parameter values for a and b are 0.34 and 0.14, respectively (Allen et al., 1998).
 278 We calibrated these parameters for every site by linear least squares regression for clear days
 279 ($R_s/R_{s0} > 0.9$) and compared the performance of both R_{nl} models (Eq. 3 and Eq. 7).

280

281

282 **2.3.2 Soil heat flux (G)**

283 The soil heat flux is commonly expressed as a fraction of R_n , particularly at large scales using
 284 remote sensing (Su, 2002; Bastiaanssen et al., 1998; Kustas et al., 1998; Kustas and Daughtry,
 285 1990; Friedl, 1996). We adopted the same approach making a distinction between daytime
 286 (F_{day}) and nighttime (F_{night}) fractions, determined by linear least squares regression between
 287 R_n and the average of the two sets of soil heat flux measurements.

288

289 **2.3.3 Aerodynamic resistance (r_a)**

290 The aerodynamic resistance under neutral stability conditions can be estimated by (Monteith
 291 and Unsworth, 1990):

292

$$293 \quad r_a = \frac{\ln \left[\frac{z_m - d}{z_{om}} \right] \ln \left[\frac{z_h - d}{z_{oh}} \right]}{k^2 u_z}, \quad 8$$

294

295 where z_m is the height of wind speed measurements [m], d is the zero plane displacement
 296 height [m], z_{om} is the roughness length governing momentum transfer [m], z_h is the height of
 297 the humidity measurements [m], z_{oh} is the roughness length governing transfer of heat and
 298 vapor [m], k is the von Karman's constant (0.41 [-]) and u_z is the wind speed at height z_m
 299 [m/s]. For grass, empirical equations are developed (FAO 56 approach) to estimate d , z_{om} and
 300 z_{oh} :

301

$$302 \quad d = 0.66V, \quad 9$$

$$303 \quad z_{om} = 0.123V, \quad 10$$

$$304 \quad z_{oh} = 0.1z_{om}, \quad 11$$

305

306 where V is the vegetation height. Wallace et al. (1984) found comparable coefficients for
 307 heather: $d = 0.63V$ and $z_{om} = 0.13V$ and therefore Eq. 9 to 11 were applied for both surfaces
 308 using a constant vegetation height of 7 and 31 cm for the grass and heather surfaces
 309 respectively. For the moss surface, we used a vegetation height of 2 cm, which is equal to the
 310 thickness of the moss mat. For the bare sand surface we assumed $d = 0$ m, and used typical
 311 surface roughness values published by Oke (1978): $z_{oh} = 0.001$ m and $z_{om} = z_{oh}$.

312

313 **2.3.4 Surface resistance (r_s) and canopy interception**

314 Canopy interception was simulated as a water storage which needs to be filled before rain
315 water reaches the soil surface. A maximum storage capacity of 0.50 mm was defined for
316 heather following the study of Ladekarl et al. (2005). To our knowledge no literature value of
317 the interception capacity of the specific grass species (*Agrostis vinealis*) is published.
318 Considering the relatively low vegetation height we assumed a maximum interception
319 capacity of 0.25 mm.

320 We distinguished wet (r_{swet}) and dry canopy surface resistance (r_s), since interception
321 water evaporates without the interference of leaf stomata. During canopy interception (i.e. if
322 the interception store is fully or partly filled) we used a surface resistance of 0 s/m, reducing
323 Eq.1 to the Penman equation (Penman, 1948; Monteith and Unsworth, 1990). After the canopy
324 storage is emptied the surface resistance switches to r_s . The r_s was back-calculated for
325 daytime periods for the heather and grass lysimeters by substituting measured R_n , G , ET_a , e_s
326 and e_a and simulated r_a into Eq. 1 under non-stressed conditions (i.e. $ET_p = ET_a$). Nighttime
327 evaporation was assumed to be equal to 0 mm. To make sure that the back-calculated r_s was
328 based on days at which evapotranspiration occurred at a potential rate, it was back-calculated
329 for every two consecutive days after precipitation events and after emptying of the
330 (calculated) interception store. The surface resistance (r_s) of bare sand and moss was assumed
331 to be equal to 10 s/m, i.e. similar to the surface resistance under well watered conditions of
332 bare soil found by Van de Griend and Owe (1994).

333 During the summer of 2013, a dry spell (from 4-7-2013 until 25-7-2013) resulted in a
334 vegetation dieback of grass and heather. Surface resistances were back-calculated for periods
335 before and after the drought event. The drought event had 22 consecutive dry days with a
336 cumulative reference evapotranspiration according to Makkink (1957) of 85 mm. Drought
337 events of similar magnitude have been recorded 12 times during the past 57 years (from 1958
338 until 2014) at climate station “de Bilt” located in the center of the Netherlands (52.1° latitude,
339 5.18° longitude), 10 km from the measurement site. The measurements in the heather
340 vegetation started a week before the drought event. During this week, there were two days
341 (30-6-2013 and 1-7-2013) for which r_s could be back-calculated. The estimated r_s for these
342 days were 35 s m⁻¹ and 107 s m⁻¹ respectively. We selected the r_s value of the second day to
343 use in our model simulations (107 s m⁻¹) because it was in close agreement with the median
344 surface resistance found by Miranda et al. (1984) of 110 s m⁻¹ in a comparable heather
345 vegetation. After the drought event, r_s increased to 331 s m⁻¹ ($N = 14$, standard error = 102 s
346 m⁻¹). For the grass vegetation the surface resistance before the drought event was 181 s m⁻¹ (N
347 = 9, standard error = 68 s m⁻¹). After the drought event the surface resistance increased to 351

348 $s\ m^{-1}$ ($N = 4$, standard error = $47\ s\ m^{-1}$). Since mosses of these habitats are desiccation tolerant
349 and quickly rehydrate after drought (Proctor et al., 2007), we didn't assess the effect of the
350 dry spell on the surface resistance of the moss surface.

351 The parameters thus obtained were used to parameterize the Penman-Monteith
352 equation and to calculate hourly ET_p values for each surface.

353

354 **2.4 Model simulations of ET_a**

355 Using hourly ET_p of the year 2013 (876 mm precipitation), we used Hydrus 1D (Šimůnek et
356 al., 2008) to simulate ET_a . If meteorological data of the local weather station was missing due
357 to snow cover or sensor maintenance, the meteorological data of weather station “de Bilt” was
358 used for the calculation of ET_p .

359 First, we simulated ET_a for the lysimeter surfaces and compared our results with the
360 lysimeter measurements of ET_a . The lower boundary condition in the model was a seepage
361 face with hydraulic pressure equal to 0 at a depth of 65 cm below the surface (50 cm soil and
362 15 cm wick). This boundary condition assumes that the boundary flux will remain zero as
363 long as the pressure head is negative. When the lower end of the soil profile becomes
364 saturated, a zero pressure head is imposed at the lower boundary and outflow calculated
365 accordingly. Second, we simulated ET_a for the groundwater-independent surroundings. We
366 expected that the availability of soil moisture in the lysimeter tanks was larger than in the
367 groundwater independent surroundings, because the lowest sections of the lysimeters need to
368 be saturated before drainage occurs. To estimate the yearly ET_a of dune vegetation in
369 environments with deep groundwater levels, we used a free drainage boundary condition (i.e.
370 a pressure head gradient of 0 and an elevation head of 1) located 2.5 m below the surface.
371 Third, we investigated the magnitude of the vegetation dieback in the summer of 2013 on
372 both ET_p and ET_a , by using two different surface resistances: one derived from the period
373 before, and one for the period after the vegetation dieback.

374 Soil hydraulic properties in the hydrological model were described by the Van
375 Genuchten relationships (Van Genuchten, 1980). Soil samples ($100\ cm^3$) collected next to
376 each lysimeter at 5 and 15 cm depth were used to derive the drying retention function. The
377 average drying retention parameters (of the two samples collected next to each lysimeter)
378 were used in the hydrological model taking hysteresis into account by assuming the wetting
379 retention curve parameter (α_{wet}) to be twice as large as the drying retention curve parameter
380 (α_{dry}) (Šimůnek et al., 1999). The unsaturated hydraulic properties (parameters l and K_0) were
381 estimated using the Rosetta database and pedotransfer functions, providing the fitted drying

382 retention curve parameters as input (Schaap et al., 2001). The hydraulic properties of the 15
383 cm long wick, guiding drainage water below the lysimeter into the tipping bucket, were taken
384 from Knutson and Selker (1994).

385 Since mosses have neither leaf stomata nor roots, ET_a from the moss surface is limited
386 by the capacity of the moss material to conduct water to the surface. This passive evaporation
387 process is similar to the process of soil evaporation, i.e. evaporation becomes limited if the
388 surface becomes too dry to deliver the potential rate. The unsaturated hydraulic properties of
389 the dense *Campylopus introflexus* moss mat covering the lysimeter soil were based on the
390 hydraulic properties derived by Voortman et al. (2013) and used in the first 2 cm of the model
391 domain. Macro pores in the moss mat were neglected by Voortman et al. (2013), which
392 implies that direct implementation of these hydraulic properties would result in large amounts
393 of surface runoff generation or ponding, since the unsaturated hydraulic conductivity (K_0) of
394 the moss mat is lower than 0.28 cm/d. Therefore, the dual porosity model of Durner (1994)
395 was used to add 1000 cm/d to the hydraulic conductivity curve of Voortman et al. (2013)
396 between -1 and 0 cm pressure head (Appendix A). This permits the infiltration of rain water at
397 high intensity rain showers without affecting the unsaturated hydraulic behavior at negative
398 pressure heads. Because of the complex shape of the retention function of the moss mat,
399 hysteresis in the soil hydraulic functions in the underlying soil was neglected for the
400 simulation of evaporation from moss surfaces. The sensitivity of this simplification on the
401 model outcomes was investigated by adjusting the soil hydraulic function of the soil from the
402 drying to the wetting curve. This had a negligible effect (<1 mm) on the simulated yearly ET_a
403 (data not shown). Besides simulations of moss evaporation with a cover of *Campylopus*
404 *introflexus*, soil physical characteristics of *Hypnum cupressiforme* were used in the first 2 cm
405 of the model domain to analyze the effect of different moss species on the water balance. Soil
406 parameters used in the model are explained in more detail in Appendix A.

407 Since the grass and heather lysimeters fully covered the soil, soil evaporation was
408 neglected for these surfaces. The root profile for the grass and heather lysimeters was 30 cm
409 deep, with the highest concentration of roots in the upper layer decreasing linearly with depth.
410 A water stress reduction function (Feddes et al., 1978) was used to simulate the closure of leaf
411 stomata during water stressed periods. Vegetation parameters are explained in more detail in
412 Appendix B. Modeled actual evapotranspiration ($ET_{a,mod}$) was aggregated to daily values and
413 compared to field measurements of ET_a during moist ($ET_{a,mod} = ET_p$) and dry conditions ($ET_{a,mod} \neq ET_p$).

415

416 2.5 Model performance assessment

417 Model performance of R_{ns} , R_{nl} , G and $ET_{a,mod}$ simulations were tested with the Nash-Sutcliffe
418 model efficiency coefficient (NSE):

419

$$420 \quad NSE = 1 - \frac{\sum_{t=1}^N (x_{o,t} - x_{m,t})^2}{\sum_{t=1}^N (x_{o,t} - \bar{x}_o)^2}, \quad 12$$

421

422 Where N is the total number of observations, $x_{m,t}$ is the model-simulated value at time step t ,
423 $x_{o,t}$ is the observed value at time step t , and \bar{x} is the mean of the observations. $NSE = 1$
424 corresponds to a perfect match of modeled to observed data. If $NSE < 0$, the observed mean is
425 a better predictor than the model. To assess the magnitude of error of model simulations, the
426 root mean squared error ($RMSE$), the mean difference (MD) and the mean percentage
427 difference ($M\%D$) were used.

428

429 3 Results and Discussion

430 3.1 Parameterization of the Penman-Monteith equation

431 3.1.1 Net shortwave radiation

432 The measured incoming and reflected solar radiation were used to compute the albedo of the
433 four surfaces by linear regression (Fig. 6; Table 5). This single value for the albedo slightly
434 overestimates the reflected solar radiation at large incoming solar radiation (Fig. 7) because of
435 a dependency of the albedo on solar elevation angle β (Yang et al., 2008; Zhang et al., 2013).
436 Nonetheless does the use of a single value for the albedo hardly affect the error in modeled
437 R_{ns} : The mean difference (MD) between measured and modeled R_{ns} lies between -0.23 and
438 1.63 Wm^{-2} (
439), which is equal to the energy required to evaporate 0.008 to 0.057 mm d^{-1} . The NSE for
440 estimating R_{ns} is close to 1 (
441), showing almost a perfect match of modeled to observed data.

442 The dense moss mat *Campylopus introflexus* entirely covers the underlying mineral
443 soil, which results in a low albedo (0.135) due to the dark green surface. The albedo of bare
444 sand (0.261) is comparable to values found in literature for bare dry coarse soils (Qiu et al.,
445 1998; Van Bavel and Hillel, 1976; Linacre, 1969; Liakatas et al., 1986) and the albedo for grass
446 (0.179) is consistent with values reported in other studies during summer time (Hollinger et
447 al., 2010) or for dried grass (Van Wijk and Scholte Ubing, 1963). Heather has a somewhat
448 lower albedo (0.078) than was found in the literature: Miranda et al. (1984) report an albedo
449 of 0.13 (*Calluna*, LAI ca. 4); Wouters et al. (1980) report an albedo of 0.102 (*Calluna*). The

450 heather vegetation in our study was in a later successional stage with aging shrubs having a
451 relatively large fraction of twigs and a smaller LAI (3.47) than found by Miranda et al.
452 (1984). Furthermore, the albedo data of heather vegetation was collected primarily past the
453 growing season from September till November. The darker surface after the growing season
454 and the lower LAI explains the small albedo compared to other studies.

455

456 **3.1.2 Net longwave radiation**

457 The fitted function of Eq. 6 describes the dynamics of the surface temperature relative to air
458 temperature (Fig. 8; Table 5). All surfaces have a similar average nighttime surface
459 temperature ($T_{s,offset}$) relative to T_a , ranging between -7.47 and -10.21°C . The solar elevation
460 angle at which the surfaces become warmer than the air temperature (μ_β), as well as the speed
461 at which the surface warms up or cools down (σ_β), are comparable between the surfaces. The
462 main difference between the surfaces is observed at high solar elevation angles. Sand and
463 moss show a clear increasing slope during the day, while grass and heather are able to
464 attenuate the increase in surface temperature, possibly due to a larger latent heat flux (Fig. 8).
465 The moss surface shows the largest increase in surface temperature during the day. Although
466 organic layers, e.g. dry peat, have a larger specific heat ($1600 \text{ J kg}^{-1}\text{K}^{-1}$) than dry sand (693 J
467 $\text{kg}^{-1}\text{K}^{-1}$) (Gavriliev, 2004), the energy required to heat up the moss material is much smaller
468 than for sand, because of the small dry bulk density of ca. 26.8 g/l (derived for *Campylopus*
469 *introflexus* from Voortman et al. (2013)). Therefore, the surface temperature and the emitted
470 longwave radiation are largest for the moss surface.

471 Our R_{nl} model (Eq. 3 and Eq. 6) simulates R_{nl} much better than the calibrated (Table 2)
472 FAO-56 R_{nl} sub-model (Table 3). For the natural grass surface, the *NSE* even becomes
473 negative using the calibrated FAO-56 approach. Several studies showed that the FAO-56 R_{nl}
474 sub-model underestimates the magnitude of R_{nl} for reference grass vegetation and poorly
475 describes the diurnal pattern (Matsui, 2010;Blonquist Jr et al., 2010;Yin et al.,
476 2008;Temesgen et al., 2007). As mentioned, the FAO-56 R_{nl} sub-model was originally
477 developed for reference grass vegetation under well-watered conditions for daily time steps,
478 but is commonly applied at hourly timescales (ASCE-EWRI, 2005;Perera et al., 2015;Gavilán
479 et al., 2008;López-Urrea et al., 2006;Irmak et al., 2005). At daily time steps, T_s is close to T_a ,
480 since the warmer daytime T_s is compensated by the cooler nighttime T_s . For hourly time steps,
481 the assumption that T_s follows T_a is not valid, which explains the poor performance of the
482 FAO-56 R_{nl} model for hourly time steps. This poor performance cannot be compensated by
483 calibrating the net emissivity parameters, since the diurnal pattern remains unaffected.

484 In this analysis a typical pattern in T_s relative to T_a is used to estimate T_s (Eq. 6), and
485 subsequently R_{nl} (Eq. 3). This relationship (Fig. 8) is sensitive to local weather conditions,
486 which implies that the parameters of Eq. 6 (Table 5) are not directly transferable to other
487 locations or climates. The applicability of the presented approach to simulate R_{nl} should be
488 tested before it is used for other surfaces or climates. It should be noted that the amount of
489 parameters that is required to simulate R_{nl} is relatively large. However, μ_β as well σ_β , are
490 comparable between the surfaces. These parameters might be assumed similar for every
491 surface, reducing the species specific model parameters to three (one more than the FAO-56
492 approach). More data of different vegetation types is required to generalize these results and
493 to assess the amount of parameters that are required to accurately simulate R_{nl} .

494

495 **3.1.3 Soil heat flux**

496 The soil heat flux G as fraction of R_n (F_{day} and F_{night}) decreases with vegetation cover (Table
497 5). The nighttime fractions are larger than the daytime fractions, as R_n becomes smaller in
498 magnitude during the night, which simultaneously corresponds to a change in direction of R_n
499 and G , from downward (positive) to upward (negative). Relatively small systematic errors are
500 made using daytime and nighttime fractions of R_n to simulate G (MD between 1.92 and 0.69
501 $W m^{-2}$) (Table 4). In remote sensing algorithms G is often simulated as fraction of R_n ,
502 depending on the LAI or the fractional vegetation cover. In e.g. the SEBS algorithm, the soil
503 heat flux fraction (F) is interpolated between 0.35 for bare soil and 0.05 for a full vegetation
504 canopy (Su, 2002). These limits are close to the bare sand (0.270) and heather (0.066) F_{day}
505 fractions (Table 5). The heather F_{day} (0.066) was close to the value found by Miranda et al.
506 (1984) of 0.04.

507 The analysis of the relationship between R_n and G was based on the average of two
508 sets of soil heat flux plates per surface. These sets of measurements showed on average a
509 good agreement: a MD below $1.07 W m^{-2}$ with a $RMSE$ ranging between 5.02 and $9.40 W m^{-2}$.

510

511 **3.1.4 Energy balance**

512 All the terms in the energy balance can be defined using daily lysimeter measurements of LE
513 and an estimate of the sensible heat flux (H) as a residual term of the energy balance. For
514 daytime measurements (between sunrise and sunset), the LE , H , G , $R_{s\uparrow}$ and R_{nl} can be
515 expressed as fraction of the $R_{s\downarrow}$. Table 6 summarizes the average fraction of $R_{s\downarrow}$ attributed to
516 these five different energy fluxes during the measurement campaign. The net longwave
517 radiation is for most surfaces the largest energy flux during daytime (Table 6).

518 The LE of most surfaces is the second largest flux during daytime, which fraction
519 increases with vegetation cover. Despite the large difference in albedo between bare sand and
520 moss, the moss surface has only a slightly larger LE fraction than bare sand (Table 6). This is
521 primarily caused by the larger R_{nl} flux of moss, which compensates the smaller amount of
522 reflected solar radiation.

523

524 **3.2 Potential and actual evapotranspiration**

525 The modeled ET_a is in agreement with the measured ET_a , with some exceptions at the onset of
526 dry out events (Fig. 9). In general, reduction of ET_p to ET_a is modeled a few days later than
527 emerges from measurements. The cumulative $ET_{a,mod}$ over the measurement period (May-
528 October 2013) deviates 21 mm (13 %), -13 mm (-7 %), 5 mm (2 %) and -3 mm (-2 %) from
529 the measured ET_a of the sand, moss, grass and heather lysimeters respectively. The results of
530 modeled vs. measured ET_a for non-water stressed ($ET_a = ET_p$) and water stresses conditions
531 ($ET_{a,mod} < ET_p$) are summarized in Table 7.

532 We did not calibrate our model, e.g. by adjusting soil hydraulic properties, because
533 several processes outlined by Allen et al. (1991) and wall flow (Cameron et al., 1992;Corwin,
534 2000;Till and McCabe, 1976;Saffigna et al., 1977) affect lysimeter measurements of ET_a and
535 drainage. We suspect that wall flow caused the slightly earlier reduction of ET_p to ET_a at the
536 onset of dry out events than was simulated by the model. Wall flow leads to a quicker
537 exfiltration of rainwater and a subsequent lower moisture content in the lysimeter, and
538 therefore a slightly earlier timing of drought compared to the model. Since wall flow does not
539 occur in the undisturbed vegetation outside the lysimeters, calibrating e.g. soil hydraulic
540 properties using measured surface and drainage fluxes in the objective function could lead to
541 biased characterizations of the soil hydraulic properties and erroneous simulations of soil
542 water flow and ET_a .

543 In our simulations, we neglected vapor flow within the soil and moss layer. Due to
544 temperature and potential gradients, vapor fluxes may occur through the soil and moss layer
545 in upward and downward direction by diffusion. Vapor flow may occur by advection as well,
546 e.g. through macro pores. Water and vapor flows act together and are hard to distinguish
547 between. Modelling and lab experiments show a minor cumulative effect of vapor flow on
548 evaporation for moist and temperate climates. Soil evaporation in a temperate climate for
549 loamy sand in Denmark was only slightly smaller (1.5 %) than a simulation excluding vapor
550 flow (Schelde et al., 1998). Experiments of Price et al. (2009) show that only 1% of the total
551 water flux was caused by vapor flow in columns of *Sphagnum* moss. Nevertheless, for a dry

552 and warm Mediterranean climate – different from ours – Boulet et al. (1997) found a
553 dominant vapor flux down to a depth of 25 cm in a bare soil during 11 days in a dry and warm
554 Mediterranean climate. Because large temperature and potential gradients occur when $ET_a \neq$
555 ET_p , vapor flow could especially become dominant in the water limited phase of evaporation.
556 We compared the model performance between dry ($ET_{a,mod} \neq ET_p$) and wet ($ET_{a,mod} = ET_p$)
557 days in Fig. 10. The model performance in both moisture conditions is comparable ($RMSE$
558 sand: dry = 0.40, wet = 0.46, $RMSE$ moss: dry = 0.30, wet = 0.39), suggesting that our
559 simplified model could describe the dominant processes and the simulation of vapor flow was
560 not required for the temperate climate of our study area.

561 One would expect oasis effects to occur in the vicinity of the lysimeters, because
562 freely draining lysimeters must saturate at the bottom of the lysimeter tank before water
563 drains out. This enlarges the water availability inside the lysimeters compared to its
564 groundwater independent surroundings and occasionally leads to a situation in which the
565 vegetation inside the lysimeters is still transpiring, while the vegetation outside the lysimeters
566 becomes water stressed and heats up. In such situation advection of sensible heat generated in
567 the vicinity of the lysimeters could contribute to the available energy for lysimeter
568 evapotranspiration. However, calculated ET_p was seldom smaller than measured lysimeter
569 ET_a , indicating that oasis effects were absent. Furthermore, if oasis effects were prominent,
570 systematic underestimation of modeled lysimeter ET_a would occur, since we ignored the
571 possible contribution of heat advection. Note that it is very unlikely that oasis effects affected
572 the back-calculated surface resistances (Table 5), since these were based on days after rain
573 events for which we may assume ET_a to be equal to ET_p for both the lysimeters and their
574 surroundings.

575 Neglecting feedbacks of drought on the transpiring leaf area and thereby the surface
576 resistance (i.e. using a fixed r_s) of heather and dry grassland vegetation leads to an
577 overestimation of cumulative ET_a of 7 to 9 % for years with relatively severe drought (Table
578 7). The delayed drought response of these vegetation types is therefore of importance to water
579 balance studies, especially when, according to the expectations, summers become dryer as a
580 result of a changing climate. Longer recordings of ET_a in heathland and grassland are required
581 to understand and parameterize the drought response of these vegetation types in coupled
582 plant physiological and hydro-meteorological models.

583 To our knowledge, this paper describes for the first time the evaporation
584 characteristics of a moss surface in a dune ecosystem in a temperate climate. The evaporation
585 rate of the dense moss mat *Campylopus introflexus* is 5 % larger than the evaporation rate of

586 bare sand. *Campylopus introflexus* forms dense moss mats and of the moss species
587 investigated by Voortman et al. (2013), it has the largest water holding capacity. Voortman et
588 al. (2013) hypothesized that moss covered soils could be more economical with water than
589 bare soils, since the unsaturated hydraulic properties of moss layers reduce the magnitude of
590 evaporation under relatively moist conditions. Our simulations of evaporation from the more
591 open structured *Hypnum cupressiforme* moss species (common in coastal dunes), which
592 primarily differs in moisture content near saturation compared to *Campylopus introflexus*
593 (0.20 instead of 0.61), confirms this hypothesis. The simulated evaporation rate for this
594 species was 29 % lower than the evaporation rate of bare soil. From both our measurements
595 and model simulations, xerophytic (drought tolerant) mosses appear to be very economical
596 with water: their evaporation rate is comparable with that of bare sand, or lower.

597 *Campylopus introflexus* is considered an invasive species in the Northern Hemisphere
598 and was first discovered in Europe in 1941 (Klinck, 2010). Considering the large difference in
599 yearly evaporation between *Hypnum cupressiforme* and *Campylopus introflexus* species (90
600 mm), the invasion of the *Campylopus introflexus* could have had negative impacts on water
601 resources in specific areas which were previously dominated by more open structured moss
602 species with poorer water retention characteristics. For sustainable management of
603 groundwater resources in coastal and inland sand dunes, an accurate estimate of the
604 groundwater recharge is required. For consultancy about the availability of water, moss
605 species cannot be categorized in a singular plant functional type, since the modulating effect
606 of the moss cover is species specific. However, in terms of water retention characteristics, the
607 species investigated by Voortman et al. (2013) are distinguished from each other by the water
608 holding capacity near saturation (θ_0 , Appendix A), which is easily measured in a laboratory.
609 Moss species could be categorized by this characteristic.

610 Mosses and lichens are common in early successional stages after colonizing and
611 stabilizing drift sand or as understory vegetation in heathlands or grasslands. Vascular plants
612 might benefit from the presence of certain moss species as more water may be conserved in
613 the root zone. On the other hand, field observations show that moss- and lichen-rich
614 vegetation can persist for many decades (Daniëls et al., 2008). Detailed measurements of
615 understory evaporation in heathlands and grasslands are required to unravel the ecological
616 interactions between mosses and vascular plants.

617

618 **4 Conclusions**

619 In this study the net longwave radiation (R_{nl}) appeared to be one of the largest energy fluxes
620 in dune vegetation. The poor performance of the calibrated FAO-56 approach for simulating
621 R_{nl} for hourly time steps illustrates that this energy flux has attracted insufficient attention in
622 evapotranspiration research. The novel approach presented in this study to simulate R_{nl}
623 outperformed the calibrated FAO-56 approach and forms an accurate alternative for
624 estimating R_{nl} .

625 A relatively simple hydrological model could be used to simulate evapotranspiration
626 of dry dune vegetation with satisfactory results. Improvements in terms of climate robustness
627 would be especially achieved if plant physiological processes were integrated in the hydro-
628 meteorological model. Without considering the effects of dry spells on the surface resistance
629 (r_s) of grassland and heathland vegetation, ET_a would be overestimated with 9 % and 7 % for
630 years with relatively severe drought (drought events with a reoccurrence of once per five
631 years).

632 Moss species are very economical with water. The evaporation of moss surfaces is
633 comparable or even lower than bare sand. By promoting moss dominated ecosystems in
634 coastal and inland dunes, the evapotranspiration could be reduced considerably, to the benefit
635 of the groundwater system. Differences in evaporation between moss species are large and
636 should be considered in water balance studies.

637 Long-term measurements of ET_a in heathland and grassland are required to study
638 feedbacks between climate and plant physiological processes in order to integrate the drought
639 response of natural vegetation in coupled plant physiological and hydro-meteorological
640 models. To understand the ecological interaction between mosses and vascular plants, detailed
641 measurements of understory evaporation in heathlands and grasslands are required.

642

643 **Acknowledgements**

644 This study was carried out within the joint research programme of the Dutch Water Utility
645 sector (<http://www.kwrwater.nl/BTO>), and the project Climate Adaptation
646 for Rural Areas (CARE), which was funded by the Knowledge for Climate Program
647 (<http://knowledgeforclimate.climateresearchnetherlands.nl/climateadaptationforruralareas>).
648 We thank the staff of Vitens for their permission to perform hydro-meteorological
649 measurements in one of their drinking water extraction sites.

650

651 **Appendix A. Soil hydraulic properties for the simulation of unsaturated flow with**
652 **Hydrus-1D**

653

654 Unsaturated flow in Hydrus 1D is described by a modified form of Richards' equation:

$$655 \quad \frac{\partial \theta}{\partial t} = \frac{\partial}{\partial z} \left(K \frac{\partial h}{\partial z} + K \right), \quad 13$$

656

657 Where K is the unsaturated conductivity [LT^{-1}], z is the vertical coordinate [L] and t is the
658 time [T]. The soil hydraulic properties were assumed to be described by the Mualum van
659 Genuchten functions:

660

$$661 \quad \theta(h) = \theta_r + \frac{\theta_0 - \theta_r}{\left[1 + |\alpha h|^n\right]^m}, \quad 14$$

662

$$663 \quad K(\theta) = K_0 S_e^l [1 - (1 - S_e^{1/m})^m]^2, \quad 15$$

664 with

$$665 \quad S_e(h) = \frac{\theta(h) - \theta_r}{\theta_0 - \theta_r}, \quad 16$$

666

667 where θ is the volumetric water content [L^3/L^3], h is the soil water pressure head [L], θ_0 is an
668 empirical parameter matching measured and modeled θ [L^3/L^3], θ_r is the residual water
669 content [L^3/L^3] and α [L^{-1}] and n [-] are empirical shape parameters of the retention function,
670 K_0 is an empirical parameter, matching measured and modeled K [LT^{-1}], S_e is the effective
671 saturation [-], l is the pore-connectivity parameter [-] and m ($=1-1/n$) [-] is an empirical
672 parameter. Drying retention data of two soil samples collected next to each lysimeter at 5 and
673 15 cm depth were used to fit a retention function with the RETC code (Van Genuchten et al.,
674 1991). Hysteresis in the retention function was accounted for by assuming the retention curve
675 parameter α for the wetting curve (α_{wet}) to be twice as large as α of the drying retention curve
676 (α_{dry}) (Šimůnek et al., 1999). The unsaturated hydraulic conductivity parameters l and K_0 were
677 estimated using the Rosetta database and pedotransfer functions, providing the fitted drying
678 retention curve parameters as input (Schaap et al., 2001). Average parameter values per
679 lysimeter are summarized in Table A1.

680 The hydraulic properties of the 15 cm long wick, guiding drainage water below the
681 lysimeter into the tipping bucket, were taken from Knutson and Selker (1994) who analyzed

682 the same brand and type of wick, i.e. Peperell ½ inch. The K_0 of the wick was adjusted to
 683 correct for the smaller cross sectional area of the wick compared to the cross sectional area of
 684 the lysimeter in the 1D model simulation. (Table A1).

685 The heterogeneous pore structure of the moss material was described by the functions
 686 of Durner (1994):

$$687 \quad S_e = w_1 \left(1 + [\alpha_1 h]^{n_1}\right)^{-m_1} + w_2 \left(1 + [\alpha_2 h]^{n_2}\right)^{-m_2}, \quad 17$$

$$688 \quad K(S_e) = K_s \frac{\left(w_1 S_{e_1} + w_2 S_{e_2}\right)^l \left(w_1 \alpha_1 \left[1 - \left(1 - S_{e_1}^{1/m_1}\right)^{m_1}\right] + w_2 \alpha_2 \left[1 - \left(1 - S_{e_2}^{1/m_2}\right)^{m_2}\right]\right)^2}{\left(w_1 \alpha_1 + w_2 \alpha_2\right)^2}, \quad 18$$

691
 692 Where w_1 and w_2 are weighting factors for two distinct pore systems of the moss layer; a
 693 capillary pore system (subscript 1) and a macro pore system active near saturation ($h > -1$ cm,
 694 subscript 2) and K_s is the hydraulic conductivity at saturation. Average hydraulic parameters
 695 of the capillary pore system and the volumetric portion of the macro pore system of the moss
 696 species *Campylopus introflexus* and *Hypnum cupressiforme* were taken from Voortman et al.
 697 (2013) (illustrated with dotted lines in Fig. A1 and Fig. A2). The α_2 parameter was fitted to
 698 the functions of Voortman et al. (2013) using $K_s = 1000$ cm/d and $n_2 = 2$ by minimizing the
 699 *RMSE* by generalized reduced gradient nonlinear optimization. Hydraulic parameter values
 700 are listed in Table A2.

701
 702 **Appendix B. Feddes function used in the Hydrus 1D model to simulate the closure of leaf**
 703 **stomata during water stressed periods.**

704
 705 The Feddes function (Feddes et al., 1978) describes the relative transpiration rate in relation to
 706 the soil water pressure head (Fig. B1) (being 0 if transpiration ceases and 1 if it equals
 707 potential rate). Near positive pressure heads, root water uptake ceases due to oxygen stress
 708 (P0). At the dry end of the function, root water uptake ceases (P3). The moment at which
 709 transpiration becomes limited due to moisture stress is dependent on the potential
 710 transpiration rate. At a high potential transpiration rate (5 mm/d in the model simulation) leaf
 711 stomata start to close earlier (P2H) than under low potential transpiration rate (P2L, 1 mm/d
 712 in the model simulation). Values for the parameters of Fig. B1 are listed in Table B1.

713 **References**

- 714 Allen, R. G., Pruitt, W. O., and Jensen, M. E.: Environmental requirements of lysimeters, in: Lysimeters for
715 evapotranspiration and environmental measurements, edited by: Allen, R. G., Howell, T. A., Pruitt, W. O., Walter, I.
716 A., and Jensen, M. E., American Society of Civil Engineers, New York, 170-181, 1991.
- 717 Allen, R. G., Pereira, L. S., Raes, D., and Smith, M.: Crop Evapotranspiration-Guidelines for Computing Crop Water
718 Requirements, FAO Irrigation and drainage paper 56. United Nations Food and Agriculture Organization, Rome,
719 1998.
- 720 ASCE-EWRI: The ASCE Standardized Reference Evapotranspiration Equation, Environmental and Water Resources
721 Institute of the American Society of Civil Engineers, Reston, Virginia, USA, 2005.
- 722 Bastiaanssen, W. G. M., Menenti, M., Feddes, R. A., and Holtslag, A. A. M.: A remote sensing surface energy balance
723 algorithm for land (SEBAL). 1. Formulation, Journal of Hydrology, 212-213, 198-212,
724 [http://dx.doi.org/10.1016/S0022-1694\(98\)00253-4](http://dx.doi.org/10.1016/S0022-1694(98)00253-4), 1998.
- 725 Blonquist Jr, J. M., Allen, R. G., and Bugbee, B.: An evaluation of the net radiation sub-model in the ASCE
726 standardized reference evapotranspiration equation: Implications for evapotranspiration prediction, Agricultural
727 Water Management, 97, 1026-1038, <http://dx.doi.org/10.1016/j.agwat.2010.02.008>, 2010.
- 728 Boulet, G., Braud, I., and Vauclin, M.: Study of the mechanisms of evaporation under arid conditions using a detailed
729 model of the soil-atmosphere continuum. Application to the EFEDA I experiment, Journal of Hydrology, 193, 114-
730 141, [http://dx.doi.org/10.1016/S0022-1694\(96\)03148-4](http://dx.doi.org/10.1016/S0022-1694(96)03148-4), 1997.
- 731 Brunt, D.: Notes on radiation in the atmosphere. I, Q. J. R. Meteorol. Soc., 58, 389-420, 10.1002/qj.49705824704,
732 1932.
- 733 Cameron, K. C., Smith, N. P., McLay, C. D. A., Fraser, P. M., McPherson, R. J., Harrison, D. F., and Harbottle, P.:
734 Lysimeters Without Edge Flow: An Improved Design and Sampling Procedure, Soil Sci. Soc. Am. J., 56, 1625-1628,
735 10.2136/sssaj1992.03615995005600050048x, 1992.
- 736 Campbell Scientific Inc.: Model HFP01SC Self-Calibrating Soil Heat Flux Plate, 24, 2014.
- 737 Corwin, D. L.: Evaluation of a simple lysimeter-design modification to minimize sidewall flow, Journal of
738 Contaminant Hydrology, 42, 35-49, [http://dx.doi.org/10.1016/S0169-7722\(99\)00088-1](http://dx.doi.org/10.1016/S0169-7722(99)00088-1), 2000.
- 739 Daniëls, F. J. A., Minarski, A., and Lepping, O.: Dominance pattern changes of a lichen-rich corynephorus grassland
740 in the inland of The Netherlands, Annali di Botanica n.s., VIII, 9-19, 2008.
- 741 Delpla, I., Jung, A. V., Baures, E., Clement, M., and Thomas, O.: Impacts of climate change on surface water quality
742 in relation to drinking water production, Environment International, 35, 1225-1233,
743 <http://dx.doi.org/10.1016/j.envint.2009.07.001>, 2009.
- 744 Dolman, A. J.: Predicting evaporation from an oak forest, Ph.D, University of Groningen, 91 pp., 1987.
- 745 Durner, W.: Hydraulic conductivity estimation for soils with heterogeneous pore structure, Water Resour. Res., 30,
746 211-223, 10.1029/93wr02676, 1994.
- 747 Feddes, R. A., Kowalik, P. J., and Zaradny, H.: Simulation of Field Water Use and Crop Yield, Pudoc Wageningen,
748 1978.
- 749 Federer, C. A., Vörösmarty, C., and Fekete, B.: Intercomparison of Methods for Calculating Potential Evaporation in
750 Regional and Global Water Balance Models, Water Resour. Res., 32, 2315-2321, 10.1029/96wr00801, 1996.
- 751 Friedl, M. A.: Relationships among Remotely Sensed Data, Surface Energy Balance, and Area-Averaged Fluxes over
752 Partially Vegetated Land Surfaces, Journal of Applied Meteorology, 35, 2091-2103, 10.1175/1520-
753 0450(1996)035<2091:rarsds>2.0.co;2, 1996.
- 754 Fuchs, M., and Tanner, C. B.: Surface Temperature Measurements of Bare Soils, Journal of Applied Meteorology, 7,
755 303-305, 10.1175/1520-0450(1968)007<0303:stmobs>2.0.co;2, 1968.
- 756 Gavilán, P., Estévez, J., and Berengena, J.: Comparison of standardized reference evapotranspiration equations in
757 Southern Spain, Journal of Irrigation and Drainage Engineering, 134, 1-12, 2008.
- 758 Gavriliev, R. I.: Thermal properties of soils and surface covers, in: Thermal Analysis, Construction, and Monitoring
759 Methods for Frozen Ground, edited by: Esch, D. C., American Society of Civil Engineers, Reston, Virginia, USA, 277-
760 295, 2004.

761 Gubler, S., Gruber, S., and Purves, R. S.: Uncertainties of parameterized surface downward clear-sky shortwave and
762 all-sky longwave radiation, *Atmos. Chem. Phys.*, 12, 5077-5098, 10.5194/acp-12-5077-2012, 2012.

763 Hollinger, D. Y., Ollinger, S. V., Richardson, A. D., Meyers, T. P., Dail, D. B., Martin, M. E., Scott, N. A.,
764 Arkebauer, T. J., Baldocchi, D. D., Clark, K. L., Curtis, P. S., Davis, K. J., Desai, A. R., Dragonik, D., Goulden, M. L.,
765 Gu, L., Katul, G. G., Pallardy, S. G., Pawu, K. T., Schmid, H. P., Stoy, P. C., Suyker, A. E., and Verma, S. B.: Albedo
766 estimates for land surface models and support for a new paradigm based on foliage nitrogen concentration, *Global
767 Change Biology*, 16, 696-710, 2010.

768 Irmak, S., Howell, T. A., Allen, R. G., Payero, J. O., and Martin, D. L.: Standardized ASCE Penman-Monteith: Impact of
769 sum-of-hourly vs. 24-hour timestep computations at reference weather station sites, *Transactions of the American
770 Society of Agricultural Engineers*, 48, 1063-1077, 2005.

771 Irmak, S., Mutibwa, D., and Payero, J. O.: Net radiation dynamics: Performance of 20 daily net radiation models as
772 related to model structure and intricacy in two climates, *Transactions of the ASABE*, 53, 1059-1076, 2010.

773 Jones, H. G.: Application of Thermal Imaging and Infrared Sensing in Plant Physiology and Ecophysiology, in:
774 *Advances in Botanical Research*, Academic Press, 107-163, 2004.

775 Kay, A. L., Bell, V. A., Blyth, E. M., Crooks, S. M., Davies, H. N., and Reynard, N. S.: A hydrological perspective on
776 evaporation: historical trends and future projections in Britain, *Journal of Water and Climate Change*, 4, 193-208,
777 doi:10.2166/wcc.2013.014, 2013.

778 Klinck, J.: NOBANIS Invasive Alien Species Fact Sheet *Campylopus introflexus*, From: Online Database of the North
779 European and Baltic Network on Invasive Alien Species - NOBANIS, 2010.

780 Knutson, J. H., and Selker, J. S.: Unsaturated hydraulic conductivities of fiberglass wicks and designing capillary wick
781 pore-water samplers, *Soil Science Society of America Journal*, 58, 721-729, 1994.

782 Kustas, W. P., and Daughtry, C. S. T.: Estimation of the soil heat flux/net radiation ratio from spectral data,
783 *Agricultural and Forest Meteorology*, 49, 205-223, [http://dx.doi.org/10.1016/0168-1923\(90\)90033-3](http://dx.doi.org/10.1016/0168-1923(90)90033-3), 1990.

784 Kustas, W. P., Zhan, X., and Schmugge, T. J.: Combining Optical and Microwave Remote Sensing for Mapping Energy
785 Fluxes in a Semiarid Watershed, *Remote Sensing of Environment*, 64, 116-131, [http://dx.doi.org/10.1016/S0034-
786 4257\(97\)00176-4](http://dx.doi.org/10.1016/S0034-4257(97)00176-4), 1998.

787 Ladekar, U. L., Rasmussen, K. R., Christensen, S., Jensen, K. H., and Hansen, B.: Groundwater recharge and
788 evapotranspiration for two natural ecosystems covered with oak and heather, *Journal of Hydrology*, 300, 76-99,
789 <http://dx.doi.org/10.1016/j.jhydrol.2004.05.003>, 2005.

790 Liakatas, A., Clark, J. A., and Monteith, J. L.: Measurements of the heat balance under plastic mulches. Part I.
791 Radiation balance and soil heat flux, *Agricultural and Forest Meteorology*, 36, 227-239,
792 [http://dx.doi.org/10.1016/0168-1923\(86\)90037-7](http://dx.doi.org/10.1016/0168-1923(86)90037-7), 1986.

793 Linacre, E. T.: Net Radiation to Various Surfaces, *Journal of Applied Ecology*, 6, 61-75, 10.2307/2401301, 1969.

794 Liu, S., Graham, W. D., and Jacobs, J. M.: Daily potential evapotranspiration and diurnal climate forcings: influence
795 on the numerical modelling of soil water dynamics and evapotranspiration, *Journal of Hydrology*, 309, 39-52, 2005.

796 López-Urrea, R., Olalla, F. M. d. S., Fabeiro, C., and Moratalla, A.: An evaluation of two hourly reference
797 evapotranspiration equations for semiarid conditions, *Agricultural Water Management*, 86, 277-282, 2006.

798 Makkink, G. G.: Testing the Penman formula by means of lysimeters, *J. Inst. Wat. Engrs.*, 11, 277-288, 1957.

799 Matsui, H.: Comparison of Net Longwave Radiation Equation in Penman-Type Evapotranspiration Equation,
800 *Transactions of The Japanese Society of Irrigation, Drainage and Rural Engineering*, 78, 531-536,
801 <http://dx.doi.org/10.11408/jsidre.78.531>, 2010.

802 Miranda, A. C., Jarvis, P. G., and Grace, J.: Transpiration and evaporation from heather Moorland, *Boundary-Layer
803 Meteorology*, 28, 227-243, 10.1007/bf00121306, 1984.

804 Monteith, J. L., and Unsworth, M. H.: *Principles of Environmental Physics*, Edward Arnold, London, 1990.

805 Moors, E. J.: *Water Use of Forest in the Netherlands*, Ph.D, Vrije Universiteit Amsterdam, 2012.

806 Nozue, K., and Maloof, J. N.: Diurnal regulation of plant growth*, *Plant, Cell & Environment*, 29, 396-408,
807 10.1111/j.1365-3040.2005.01489.x, 2006.

808 Oke, T. R.: *Boundary Layer Climates*, Methuen & Co Ltd, London, 372 pp., 1978.

809 Penman, H. L.: Natural evaporation from open water, bare soil and grass, *Proceedings of the Royal Society of London*
810 *Series a-Mathematical and Physical Sciences*, 193, 120-145, 10.1098/rspa.1948.0037, 1948.

811 Perera, K. C., Western, A. W., Nawarathna, B., and George, B.: Comparison of hourly and daily reference crop
812 evapotranspiration equations across seasons and climate zones in Australia, *Agricultural Water Management*, 148,
813 84-96, <http://dx.doi.org/10.1016/j.agwat.2014.09.016>, 2015.

814 Price, J. S., Edwards, T. W. D., Yi, Y., and Whittington, P. N.: Physical and isotopic characterization of evaporation
815 from Sphagnum moss, *Journal of Hydrology*, 369, 175-182, 2009.

816 Proctor, M. C. F., Oliver, M. J., Wood, A. J., Alpert, P., Stark, L. R., Cleavitt, N. L., and Mishler, B. D.: Desiccation-
817 tolerance in bryophytes: A review, *The Bryologist*, 110, 595-621, 10.1639/0007-
818 2745(2007)110[595:DIBAR]2.0.CO;2, 2007.

819 Qiu, G. Y., Yano, T., and Momii, K.: An improved methodology to measure evaporation from bare soil based on
820 comparison of surface temperature with a dry soil surface, *Journal of Hydrology*, 210, 93-105, 1998.

821 Saffigna, P. G., Kenney, D. R., and Tanner, C. B.: Lysimeter and field measurements of chloride and bromide leaching
822 in an uncultivated loamy sand, *Soil Sci. Soc. Am. J.*, 41, 478-482, 1977.

823 Saito, H., and Šimůnek, J.: Effects of meteorological models on the solution of the surface energy balance and soil
824 temperature variations in bare soils, *Journal of Hydrology*, 373, 545-561,
825 <http://dx.doi.org/10.1016/j.jhydrol.2009.05.019>, 2009.

826 Schaap, M. G., Leij, F. J., and Van Genuchten, M. T.: Rosetta: A computer program for estimating soil hydraulic
827 parameters with hierarchical pedotransfer functions, *Journal of Hydrology*, 251, 163-176, 10.1016/S0022-
828 1694(01)00466-8, 2001.

829 Schelde, K., Thomsen, A., Heidmann, T., Schjønning, P., and Jansson, P. E.: Diurnal fluctuations of water and heat
830 flows in a bare soil, *Water Resources Research*, 34, 2919-2929, 10.1029/98wr02225, 1998.

831 Shuttleworth, W. J.: Putting the 'vap' into evaporation, *Hydrology and Earth System Sciences*, 11, 210-244, 2007.

832 Šimůnek, J., Kodešová, R., Gribb, M. M., and van Genuchten, M. T.: Estimating hysteresis in the soil water retention
833 function from cone permeameter experiments, *Water Resources Research*, 35, 1329-1345, 10.1029/1998wr900110,
834 1999.

835 Šimůnek, J., Šejna, M., Saito, H., Sakai, M., and van Genuchten, M. T.: The Hydrus-1D Software Package for
836 Simulating the movement of water, heat, and multiple solutes in variably saturated media, version 4.0, HYDRUS
837 Software Series 3, Department of Environmental Sciences, University of California Riverside, Riverside, 2008.

838 Su, Z.: The Surface Energy Balance System (SEBS) for estimation of turbulent heat fluxes, *Hydrology and Earth*
839 *System Sciences*, 6, 85-99, 2002.

840 Temesgen, B., Eching, S., and Frame, K.: Comparing net radiation estimation methods: CIMIS versus Penman-
841 Monteith, *Journal of Irrigation and Drainage Engineering*, 133, 265-271, 10.1061/(ASCE)0733-
842 9437(2007)133:3(265), 2007.

843 Till, A. R., and McCabe, T. P.: Sulfur leaching and lysimeter characterization, *Soil Sci.*, 121, 44-47, 1976.

844 Van Bavel, C. H. M., and Hillel, D. I.: Calculating potential and actual evaporation from a bare soil surface by
845 simulation of concurrent flow of water and heat, *Agricultural Meteorology*, 17, 453-476,
846 [http://dx.doi.org/10.1016/0002-1571\(76\)90022-4](http://dx.doi.org/10.1016/0002-1571(76)90022-4), 1976.

847 Van de Griend, A. A., and Owe, M.: Bare soil surface resistance to evaporation by vapor diffusion under semiarid
848 conditions, *Water Resources Research*, 30, 181-188, 10.1029/93wr02747, 1994.

849 Van Genuchten, M. T.: A closed-form equation for predicting the hydraulic conductivity of unsaturated soils, *Soil*
850 *Science Society of America Journal*, 44, 892-898, 10.2136/sssaj1980.03615995004400050002x, 1980.

851 Van Genuchten, M. T., Leij, F. J., and Yates, S. R.: The RETC Code for Quantifying the Hydraulic Functions of
852 Unsaturated Soils, Version 1.0, Salinity Laboratory, USDA, ARS, Riverside, California, 1991.

853 van Vliet, M. T. H., and Zwolsman, J. J. G.: Impact of summer droughts on the water quality of the Meuse river,
854 *Journal of Hydrology*, 353, 1-17, <http://dx.doi.org/10.1016/j.jhydrol.2008.01.001>, 2008.

855 Van Wijk, W. R., and Scholte Ubing, D. W.: Radiation, in: *Physics of plant environment*, edited by: Van Wijk, W. R.,
856 North-Holland Publishing, Amsterdam, The Netherlands, 62-101, 1963.

857 Voortman, B. R., Bartholomeus, R. P., Van Bodegom, P. M., Gooren, H., Van Der Zee, S. E. A. T. M., and Witte, J. P. M.:
858 Unsaturated hydraulic properties of xerophilous mosses: towards implementation of moss covered soils in
859 hydrological models, *Hydrological Processes*, 2013.

860 Wallace, J. S., Lloyd, C. R., Roberts, J., and Shuttleworth, W. J.: A comparison of methods for estimating aerodynamic
861 resistance of heather (*Calluna vulgaris* (L.) Hull) in the field, *Agricultural and Forest Meteorology*, 32, 289-305,
862 [http://dx.doi.org/10.1016/0168-1923\(84\)90055-8](http://dx.doi.org/10.1016/0168-1923(84)90055-8), 1984.

863 Wouters, D. S., Keppens, H., and Impens, I.: Factors determining the longwave radiation exchange over natural
864 surfaces, *Arch. Met. Geoph. Biokl. B.*, 28, 63-71, 10.1007/bf02243835, 1980.

865 Yang, F., Mitchell, K., Hou, Y.-T., Dai, Y., Zeng, X., Wang, Z., and Liang, X.-Z.: Dependence of Land Surface Albedo on
866 Solar Zenith Angle: Observations and Model Parameterization, *Journal of Applied Meteorology and Climatology*, 47,
867 2963-2982, 10.1175/2008JAMC1843.1, 2008.

868 Yin, Y., Wu, S., Zheng, D., and Yang, Q.: Radiation calibration of FAO56 Penman-Monteith model to estimate
869 reference crop evapotranspiration in China, *Agricultural Water Management*, 95, 77-84,
870 10.1016/j.agwat.2007.09.002, 2008.

871 Zhang, Y.-f., Wang, X.-p., Hu, R., Pan, Y.-x., and Zhang, H.: Variation of albedo to soil moisture for sand dunes and
872 biological soil crusts in arid desert ecosystems, *Environ Earth Sci*, 1-8, 10.1007/s12665-013-2532-7, 2013.

873 Zhou, M. C., Ishidaira, H., Hapuarachchi, H. P., Magome, J., Kiem, A. S., and Takeuchi, K.: Estimating potential
874 evapotranspiration using Shuttleworth-Wallace model and NOAA-AVHRR NDVI data to feed a distributed hydrological
875 model over the Mekong River basin, *J Hydrol*, 327, 151-173, 2006.

876 Zwolsman, J. J. G., and van Bokhoven, A. J.: Impact of summer droughts on water quality of the Rhine River - A
877 preview of climate change?, 56, 45-55, 2007.

878

879

880 Table 1. Model performance of R_{ns} simulations

| Surface | <i>N</i> | <i>NSE</i> | <i>RMSE</i> [Wm ⁻²] | <i>MD</i> [Wm ⁻²] | <i>M%D</i> [%] |
|----------------|----------|------------|------------------------------------|----------------------------------|-------------------|
| Sand | 218 | 0.998 | 5.99 | -0.23 | -0.10 |
| Moss | 1317 | 0.999 | 5.46 | 1.18 | 0.46 |
| Grass | 1203 | 0.998 | 7.78 | 1.63 | 0.55 |
| Heather | 407 | 0.999 | 3.00 | 0.24 | 0.09 |

881

882

883 Table 2. Calibrated net emissivity parameters of the FAO-56 R_{nl} sub-model (Eq. 7).

| | <i>a</i> | <i>b</i> |
|---------|----------|----------|
| Sand | 0.31 | -0.00 |
| Moss | 0.33 | 0.02 |
| Grass | 0.36 | -0.06 |
| Heather | 0.24 | 0.02 |

884

885

886 Table 3. Model performance of R_{nl} simulations for hourly time steps.

| Surface | <i>N</i> | <i>NSE</i> | <i>RMSE</i> [Wm⁻²] | <i>MD</i> [Wm⁻²] | <i>M%D</i> [%] |
|---------------------------|-----------------|-------------------|--|--|---------------------------|
| Using Eq. 3 | | | | | |
| Sand | 5891 | 0.65 | 27.37 | 0.92 | 1.52 |
| Moss | 5997 | 0.74 | 28.57 | 3.73 | 5.19 |
| Grass | 6113 | 0.71 | 25.66 | 1.41 | 2.36 |
| Heather | 2424 | 0.63 | 27.63 | -0.21 | -0.40 |
| Using FAO-56 Eq. 7 | | | | | |
| Sand | 5891 | 0.41 | 35.39 | 4.34 | 7.14 |
| Moss | 5997 | 0.31 | 46.67 | 14.84 | 20.65 |
| Grass | 6113 | -0.07 | 49.41 | -18.23 | -30.38 |
| Heather | 2424 | 0.29 | 38.24 | 10.50 | 19.54 |

887

888

889 Table 4. Model performance of G simulations.

| Surface | N | NSE | $RMSE$ [Wm ⁻²] | MD [Wm ⁻²] | $M\%D$ [%] |
|----------------|------|-------|-------------------------------|-----------------------------|---------------|
| Sand | 6080 | 0.820 | 20.06 | 1.92 | 22.16 |
| Moss | 5335 | 0.901 | 12.02 | 1.65 | 24.29 |
| Grass | 6046 | 0.868 | 8.97 | 1.60 | 43.42 |
| Heather | 2028 | 0.641 | 11.39 | 0.69 | 40.27 |

890

891

892

893 Table 5. Parameters of the four different surfaces used for the calculation of ET_p for hourly
894 time steps.

| Parameter | Sand | Moss | Grass | Heather |
|---|-------------|-------------|--------------|----------------|
| albedo [-] | 0.261 | 0.135 | 0.179 | 0.078 |
| μ_β [radians] | 0.10 | 0.10 | 0.13 | 0.09 |
| σ_β [radians] | 0.09 | 0.09 | 0.11 | 0.08 |
| $T_{s,amp}$ [°C] | 11.26 | 14.21 | 19.70 | 15.89 |
| $T_{s,offset}$ [°C] | -7.47 | -8.14 | -10.21 | -9.67 |
| $T_{s,slope}$ [°C radians ⁻¹] | 7.83 | 11.82 | 0.00 | 0.00 |
| F_{day} [-] | 0.270 | 0.211 | 0.129 | 0.066 |
| F_{night} [-] | 0.761 | 0.647 | 0.527 | 0.462 |
| r_{swet} [s m ⁻¹] | --- | --- | 0 | 0 |
| r_s [s m ⁻¹] before drought | 10 | 10 | 181 | 107 |
| r_s [s m ⁻¹] after drought | 10 | 10 | 351 | 331 |

895

896

897 Table 6. Average fractionation of the incoming shortwave radiation ($R_{s\downarrow}$) between different
 898 energy fluxes during daytime.

| Surface | <i>LE</i> | <i>H</i> | <i>G</i> | $R_{s\uparrow}$ | R_{nl} |
|----------------|------------------|-----------------|-----------------|-----------------------------------|----------------------------|
| Sand | 0.22 | 0.13 | 0.10 | 0.26 | 0.28 |
| Moss | 0.24 | 0.17 | 0.09 | 0.14 | 0.36 |
| Grass | 0.27 | 0.21 | 0.06 | 0.18 | 0.29 |
| Heather | 0.35 | 0.20 | 0.05 | 0.08 | 0.32 |

899

900

901 Table 7. Modeled ET_p and ET_a for different surfaces in a lysimeter (lys.) and for a situation
 902 with deep groundwater levels (gw. ind.) for the year 2013.

| | ET_p (mm) | ET_a lys. (mm) | ET_a gw. ind. (mm) |
|---------------------------------|-------------|------------------|----------------------|
| Bare sand | 400 | 295 | 258 |
| Moss (<i>Campylopus int.</i>) | 468 | 312 | 272 |
| Moss (<i>Hypnum cup.</i>) | 468 | --- | 182 |
| Grass | 392 | 350 | 333 |
| Grass no dieback | 429 (+9%) | 382 (+9%) | 362 (+9%) |
| Heather | 549 | 460 | 391 |
| Heather no dieback | 610 (+11%) | 499 (+8%) | 420 (+7%) |

903

904

905 Table A1. Hydraulic parameter values of lysimeter soils.

| | θ_r | θ_0 | α_{dry} | α_{wet} | n | K_0 | L |
|-----------|------------|------------|-----------------------|-----------------------|-------|--------|--------|
| | [-] | [-] | [cm ⁻¹] | [cm ⁻¹] | [-] | [cm/h] | [-] |
| Bare Sand | 0.01 | 0.367 | 0.023 | 0.046 | 2.945 | 1.042 | -0.401 |
| Moss | 0.01 | 0.397 | 0.019 | --- | 2.335 | 0.734 | -0.173 |
| Grass | 0.01 | 0.401 | 0.025 | 0.050 | 2.071 | 1.119 | -0.278 |
| Heather | 0.01 | 0.392 | 0.018 | 0.036 | 2.581 | 0.679 | -0.186 |
| Wick | 0.00 | 0.630 | 0.098 | 0.196 | 3.610 | 2.180 | 0.500 |

906

907

908 Table A2. Hydraulic parameter values of the two moss species.

| | θ_r | θ_s | α_1 | n | K_s | l | w_2 | α_2 | n_2 |
|------------------------|------------|------------|---------------------|------|--------|-------|-------|---------------------|-------|
| | [-] | [-] | [cm ⁻¹] | [-] | [cm/h] | [-] | [-] | [cm ⁻¹] | [-] |
| <i>Campylopus int.</i> | 0.060 | 0.936 | 0.080 | 2.25 | 41.67 | -2.69 | 0.371 | 45.89 | 2.00 |
| <i>Hypnum cup.</i> | 0.010 | 0.971 | 0.013 | 2.17 | 41.67 | -2.37 | 0.800 | 16.61 | 2.00 |

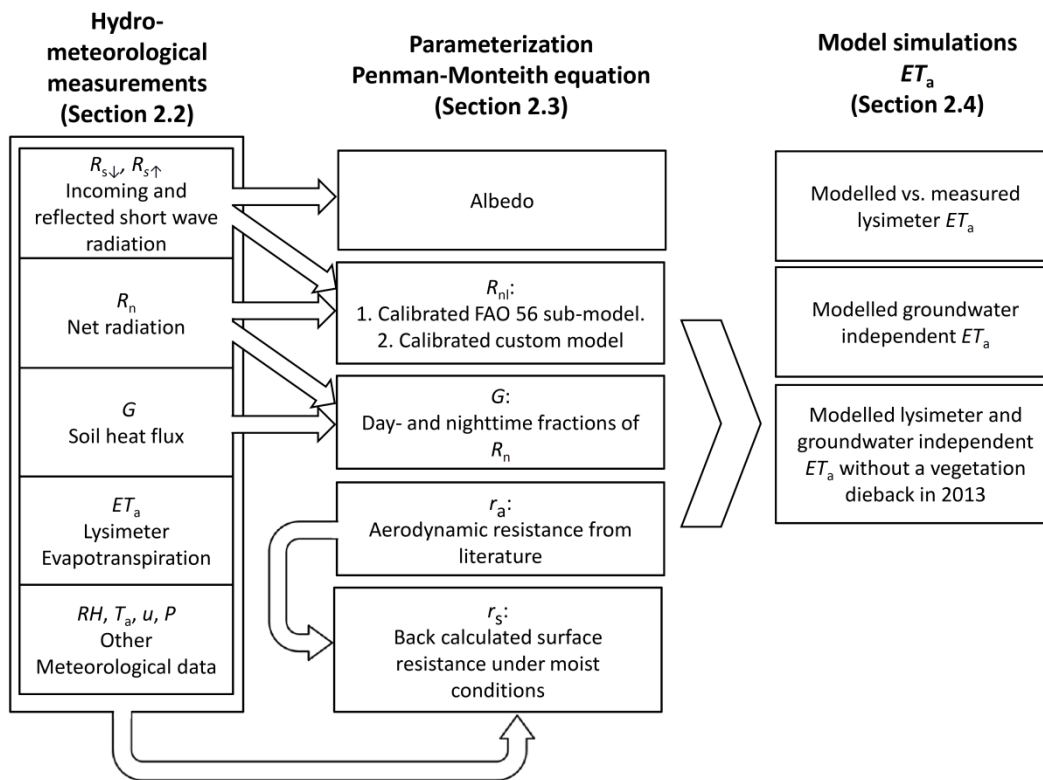
909

910

911 Table B1. Parameters of the water stress reduction function used in the Hydrus 1D model.

| P0 | P1 | P2H | P2L | P3 | r2H | r2L |
|------|------|------|-------|-------|--------|--------|
| [cm] | [cm] | [cm] | [cm] | [cm] | [mm/h] | [mm/h] |
| -10 | -25 | -300 | -1000 | -8000 | 5 | 1 |

912



913

914 Fig. 1. Organization of the research from measurements to model simulations.

915

916

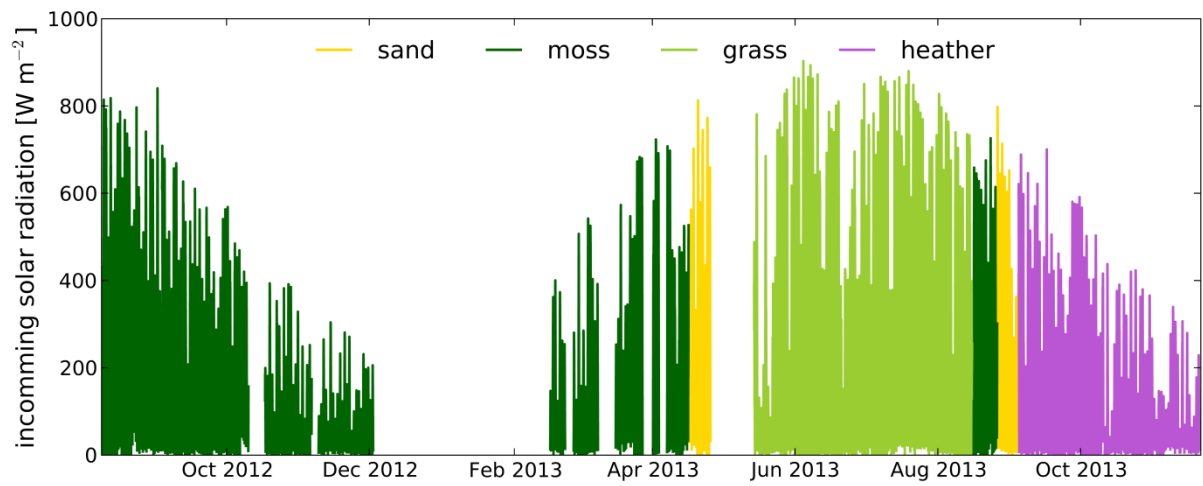


917

918 Fig. 2. The vegetation types studied in this paper, a) the moss surface with an approximately 2
919 cm thick layer of *Campylopus introflexus* (inset), b) the grass surface, primarily *Agrostis*
920 *vinealis* and c) the heather surface, *Calluna vulgaris*.

921

922

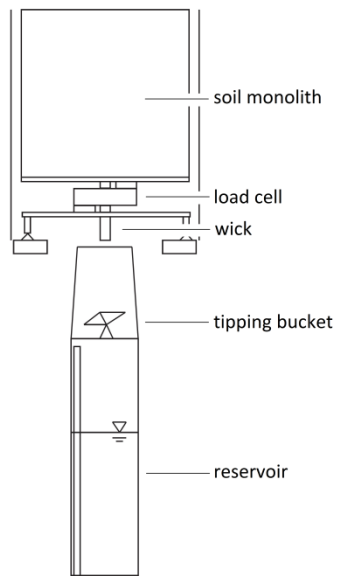


923

924 Fig. 3. Measured incoming solar radiation $R_{s\downarrow}$ at the four different surfaces. Periods with snow

925 cover or sensor maintenance were omitted.

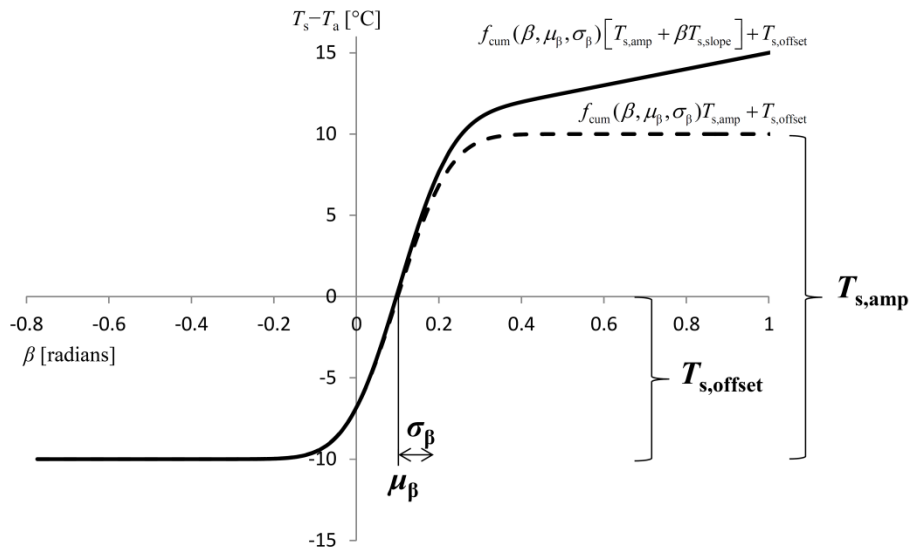
926



927

928 Fig. 4. Lysimeter design.

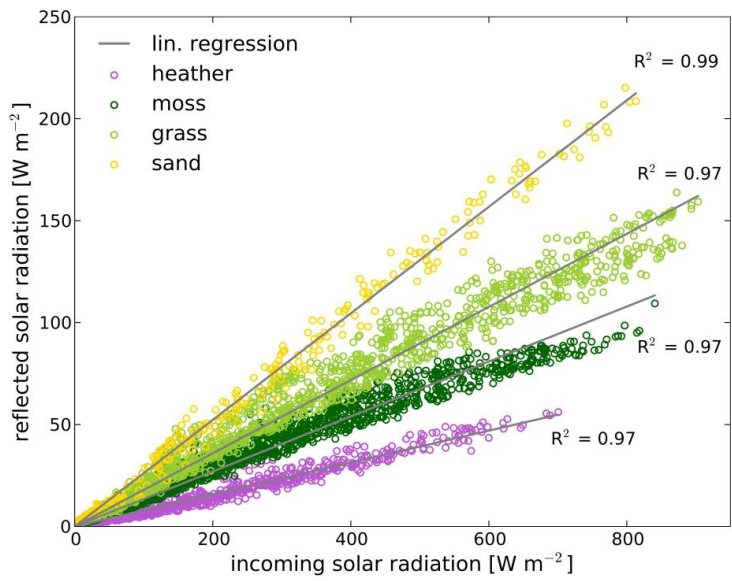
929



930

931 Fig. 5. Eq. 6 and associated parameters to describe the surface-air temperature difference,
 932 substituted for T_s in R_{nl} (Eq. 3).

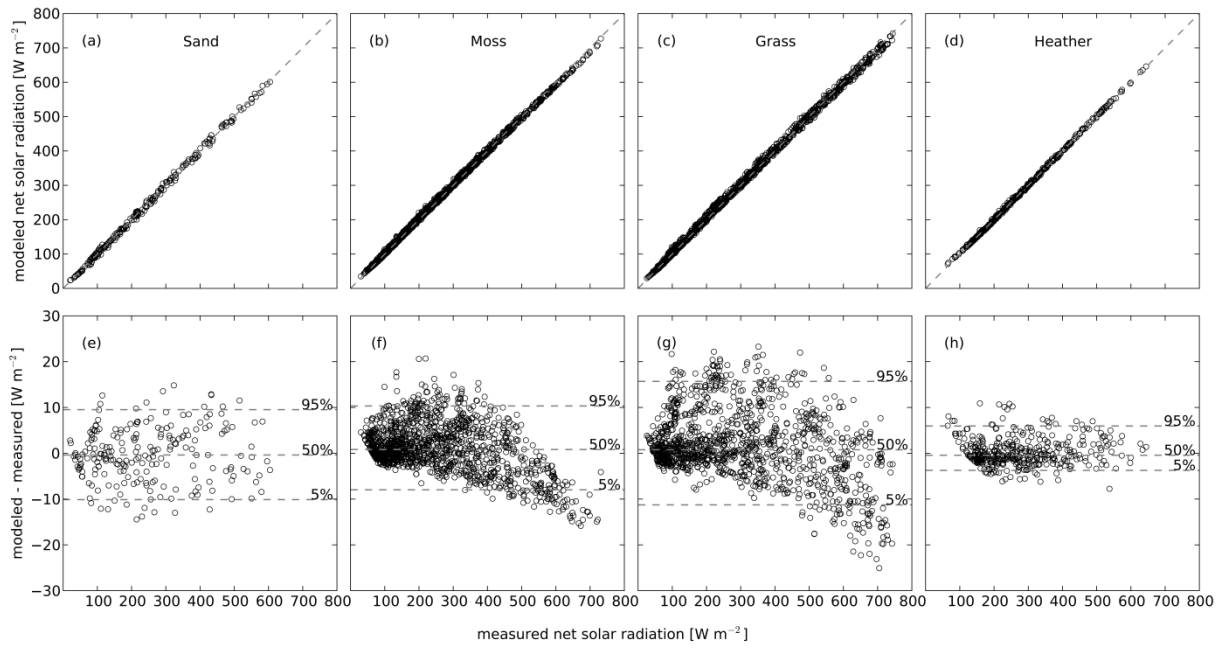
933



934

935 Fig. 6. Linear regressions between incoming and reflected solar radiation.

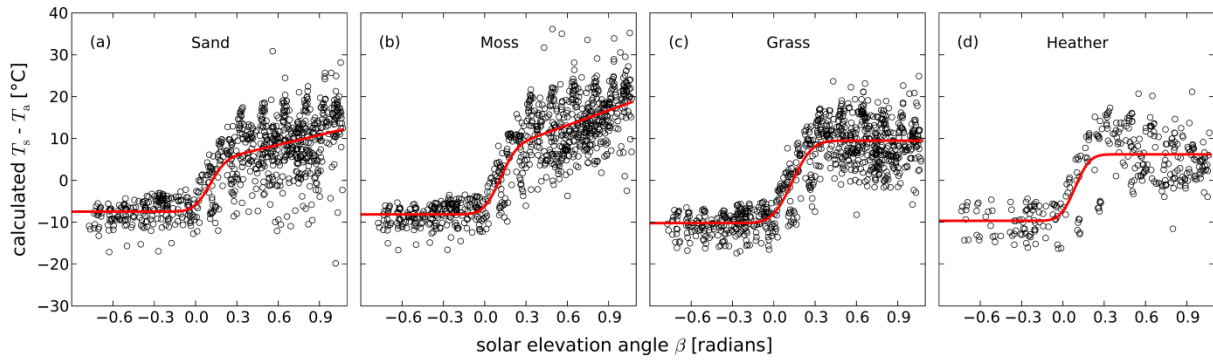
936



937

938 Fig. 7. Modeled compared to measured net solar radiation (figures a- d, dashed lines are 1:1
 939 lines) and deviations from the 1:1 line (figures e- h, dashed lines indicate 5, 50 and 95
 940 percentiles).

941

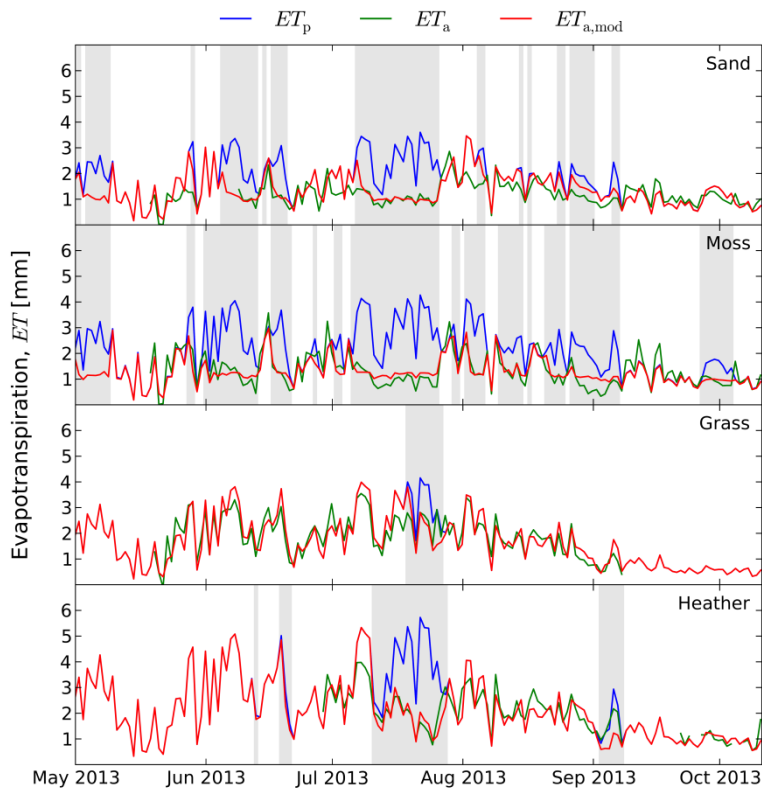


942

943 Fig. 8. Measured surface temperature relative to air temperature ($T_s - T_a$) for clear hours ($f_{cd} >$
 944 0.9) as function of solar elevation angle β . Relationships (red lines) were fitted to the data
 945 using Eq. 6.

946

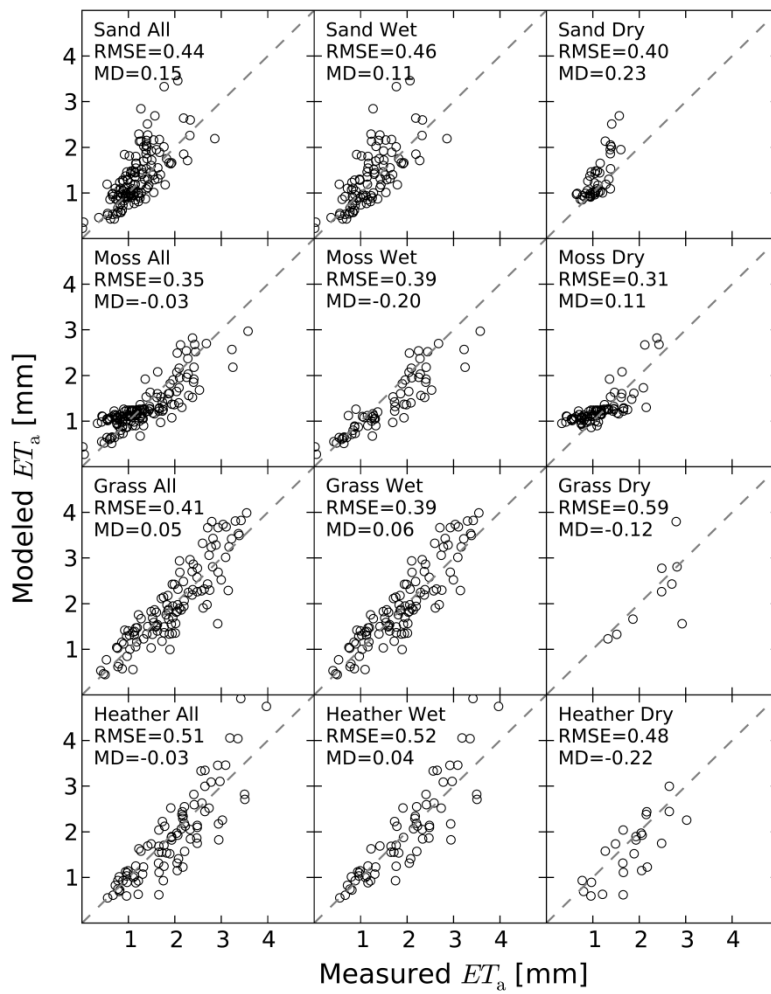
947



948

949 Fig. 9. Measured and modeled daily ET for the four lysimeters. Grey bars indicate time
950 periods where $ET_{a,mod}$ is smaller than ET_p , i.e. when evapotranspiration was water limited.

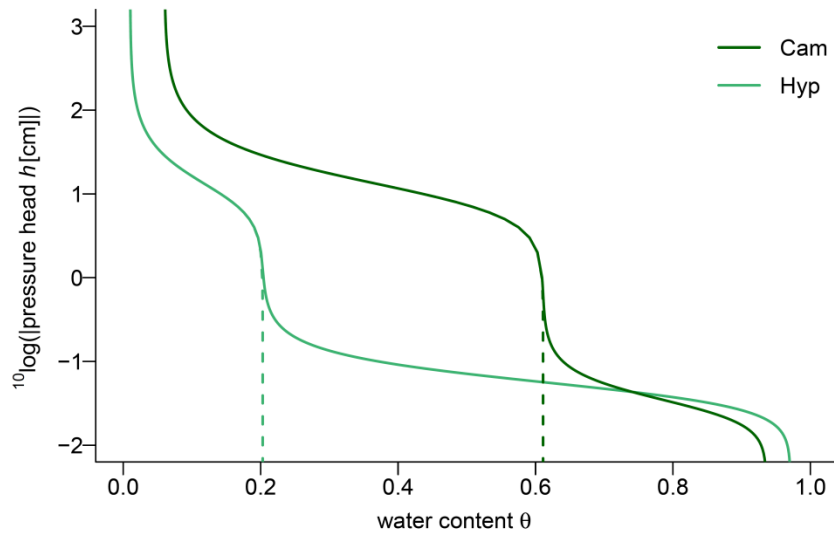
951



953

954 Fig. 10. Measured vs. modeled ET_a of the lysimeters for all, wet ($ET_{a,mod} = ET_p$) and dry
 955 ($ET_{a,mod} \neq ET_p$) days. Dotted lines represent the 1:1 lines.

956

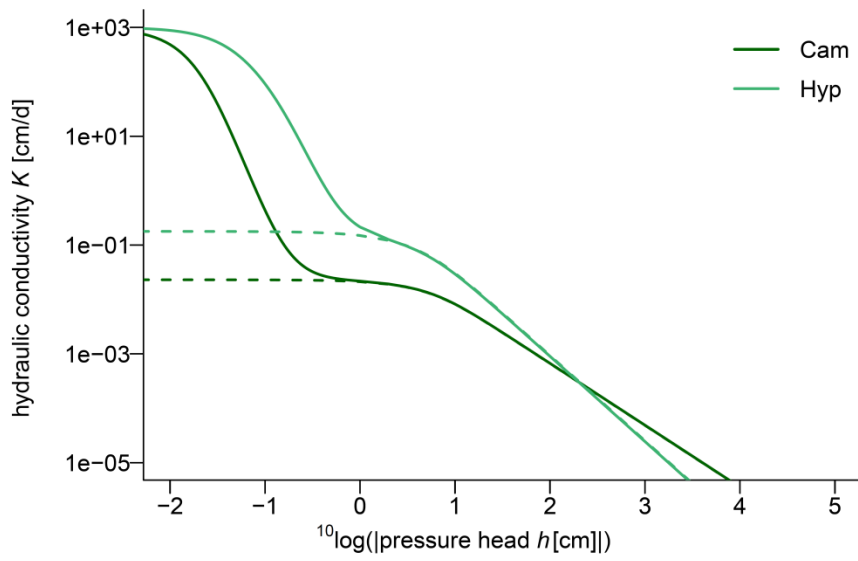


957

958 Fig. A1. Water retention functions of two moss species: *Campylopus introflexus* and *Hypnum*
 959 *cupressiforme*. The dotted lines indicate the contribution of the capillary pore system
 960 characterized by Voortman et al. (2013).

961

962

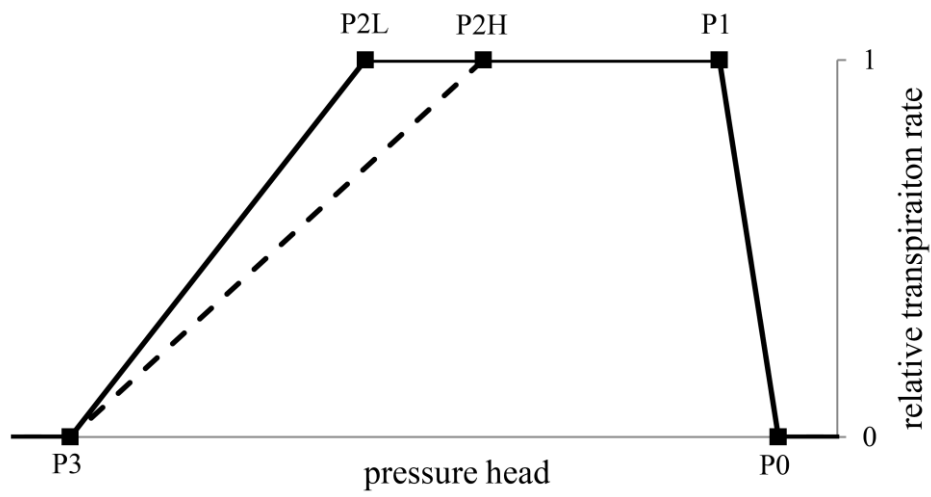


963

964 Fig. A2. Hydraulic conductivity functions for two moss species: *Campylopus introflexus* and
965 *Hypnum cupressiforme*. The dotted lines indicate the contribution of the capillary pore system
966 characterized by Voortman et al. (2013).

967

968



969

970 Fig. B1. The relative transpiration rate as function of soil water pressure head according to
971 Feddes et al. (1978).

972